Structural Basis of Tubulin Recruitment and Assembly by Microtubule Polymerases with Tumor Overexpressed Gene (TOG) Domain Arrays

Stanley Nithianantham[1], Brian D Cook[1], Madeleine Beans[1], Fei Guo[1], Fred Chang[2], Jawdat Al-Bassam[1]

[1]Molecular Cellular Biology Department, University of California, Davis, CA. [2]Department of Cell and Tissue Biology University of California, San Francisco, CA.

Abstract:

XMAP215/Stu2/Alp14 proteins accelerate microtubule plus-end polymerization by recruiting tubulins via arrays of Tumor Overexpressed Gene (TOG) domains, yet their mechanism remains unknown. Here, we describe the biochemical and structural basis for TOG arrays in recruiting and polymerizing tubulins. Alp14 binds four tubulins via dimeric TOG1-TOG2 subunits, in which each domain exhibits a distinct exchange rate for tubulin. X-ray structures revealed square-shaped assemblies composed of pseudo-dimeric TOG1-TOG2 subunits assembled head-to-tail, positioning four unpolymerized tubulins in a polarized wheel-like configuration. Crosslinking and electron microscopy show Alp14-tubulin forms square assemblies in solution, and inactivating their interfaces destabilize this organization without influencing tubulin binding. An X-ray structure determined using approach to modulate tubulin polymerization revealed an unfurled assembly, in which TOG1-TOG2 uniquely bind to two polymerized tubulins. Our findings suggest a new microtubule polymerase model in which TOG arrays recruit tubulins by forming square assemblies that then unfurl, facilitating their concerted polymerization into protofilaments.

Introduction:

Microtubules (MTs) are highly dynamic polarized polymers that perform critical and diverse cellular functions including formation of bipolar mitotic spindles, intracellular organization, and modulation of cell development and cell migration (Akhmanova and Steinmetz, 2008, 2015). MTs are assembled from αβ-tubulin heterodimers (herein termed αβ-tubulin), and their polymerization exhibits dynamic instability arising from guanosine triphosphate (GTP) hydrolysis in β-tubulins at MT ends. However, the conformational changes promoting soluble αβ-tubulins to polymerize at MT ends remain poorly understood. Polymerization of αβ-tubulin and GTP hydrolysis are regulated by conserved proteins that bind at MT plus-ends or along MT lattices (Akhmanova and Steinmetz, 2008, 2011, 2015; Al-Bassam and Chang, 2011; Al-Bassam et al., 2010; Brouhard and Rice, 2014). The XMAP215/Stu2/Alp14 MT polymerases are among the best-studied families of MT regulators. They localize to the extreme tips of MT plus-ends and accelerate αβ-tubulin polymerization in eukaryotes (Akhmanova and Steinmetz, 2011, 2015; Al-Bassam and Chang, 2011; Maurer et al., 2014). Loss or depletion of MT polymerases is lethal in most eukaryotes as it severely decreases MT polymerization rates during interphase, resulting in shortened mitotic spindles (Al-Bassam et al., 2012; Cullen et al., 1999; Wang and Huffaker, 1997). MT polymerases also bind kinetochores, where they accelerate MT dynamics and regulate kinetochore-MT attachment (Miller et al., 2016; Tanaka et al., 2005). MT polymerases recruit αβ-tubulins via arrays of conserved Tumor Overexpressed Gene (TOG) domains (herein termed TOG arrays), which are critical for their

function (Reber et al., 2013; Widlund et al., 2011). Arrays of TOG-like domains are conserved in two other classes of MT regulators, CLASP and Crescerin/CHE-12 protein families (Al-Bassam and Chang, 2011; Al-Bassam et al., 2010; Das et al., 2015), suggesting that arrays of TOG domains uniquely evolved to regulate diverse MT polymerization functions through the binding of αβ-tubulins in various intracellular settings.

Yeast MT polymerases, such as *Saccharomyces cerevisiae* Stu2p and *Schizosccharomyces pombe* Alp14, are homodimers containing two unique and conserved TOG domain classes, TOG1 and TOG2, per subunit, numbered based on their proximity to the N-terminus in the protein sequence. In contrast, metazoan orthologs, such as XMAP215 and ch-TOG, are monomers with five tandem TOG domains, TOG1 through TOG5 (Al-Bassam and Chang, 2011; Brouhard and Rice, 2014). Phylogenetic analyses suggest that TOG1 and TOG2 domains are evolutionarily distinct (Al-Bassam and Chang, 2011), and that TOG3 and TOG4 domains in metazoans are evolutionarily and structurally exclusively related to the TOG1 and TOG2 domains, respectively (Brouhard et al., 2008; Fox et al., 2014; Howard et al., 2015). Thus, despite differences in TOG array organization in yeast and metazoan proteins, both groups contain an array of tandem TOG1-TOG2 domains.

Structural studies contributed to our understanding of the molecular basis of TOG domain function in recruiting soluble αβ-tubulin. Each TOG domain is composed

of six α-helical HEAT (Huntingtin, EF3A, ATM, and TOR) repeats, which form a conserved paddle-shaped structure (Al-Bassam and Chang, 2011; Al-Bassam et al., 2007; Al-Bassam et al., 2006; Brouhard and Rice, 2014; Slep and Vale, 2007). X-ray structures of isolated TOG1 and TOG2 domains in complex with αβ-tubulins revealed that these domains recognize the curved αβ-tubulin conformations via inter-helical loops positioned along an edge of these paddle-shaped domains (Ayaz et al., 2014; Ayaz et al., 2012). Straightening of the curved αβ-tubulins upon polymerization into MTs likely dissociates TOG domains from the complexes. Our previous studies indicate that native TOG arrays from yeast or metazoan MT polymerases assemble into discrete particle-like assemblies upon binding αβ-tubulin (Al-Bassam and Chang, 2011; Al-Bassam et al., 2006). Both TOG1 and TOG2 domains are critical for MT polymerase function, and their inactivation results in MT functional defects (Al-Bassam et al., 2012; Al-Bassam et al., 2006; Ayaz et al., 2014). Two models were proposed to explain how arrays of TOG domains function as MT polymerases. One model based on studies of native TOG arrays indicates that they may form ordered assemblies upon binding αβ-tubulins (Al-Bassam et al., 2006; Brouhard et al., 2008). A second model, based on studies of isolated TOG domains or short TOG arrays, suggests that these arrays form flexible assemblies in which TOG1 and TOG2 independently recruit multiple αβ-tubulins to MT plus-ends (Al-Bassam and Chang, 2011; Ayaz et al., 2014). Distinguishing between these models requires understanding the high-resolution organization of native TOG arrays in complex with αβ-tubulin and their transitions during αβ-tubulin recruitment and

polymerization phases.

Here, we describe biochemical and structural states of TOG arrays during αβ-tubulin recruitment and polymerization states. We show that the yeast MT polymerase, Alp14, recruits four αβ-tubulins using dimeric arrays of TOG1-TOG2 domains. TOG1 and TOG2 domains each bind and release αβ-tubulins with different rates. X-ray structures reveal pseudo-dimeric TOG1-TOG2 subunits in head-to-tail square-shaped assemblies, each of which orients four unpolymerized αβ-tubulins in a polarized configuration. Crosslinking and mass spectrometry and electron microscopy studies show that dimeric yeast TOG arrays form these square assemblies in solution. Alp14 mutants with inactivated binding interfaces show disorganized configurations or polymerized arrangements, but without any defects in αβ-tubulin binding. Using a novel approach to promote the limited polymerization of αβ-tubulins while bound to TOG arrays, we determined an X-ray structure of an “unfurled” TOG1-TOG2 array:αβ-tubulin assembly revealing TOG1 and TOG2 bound to two αβ-tubulins polymerized head-to-tail into a protofilament. Our studies establish a new “polarized unfurling” model for TOG arrays as MT polymerases.

Results

TOG1 and TOG2 domains possess distinct affinities for αβ-tubulin

The *S. pombe* Alp14 is a typical yeast MT polymerase, consisting of a tandem array of N-terminal TOG1 and TOG2 domains separated by a 60-residue linker,

followed by a Ser-Lys-rich (SK-rich) region and a C-terminal coiled-coil domain that regulates dimerization (Figure 1A). We studied the αβ-tubulin binding capacities and stoichiometries of near native monomeric and dimeric Alp14, which both consist of TOG1-TOG2 arrays and differ by the presence of a C-terminal SK-rich region and dimerization coiled-coil domain. Using quantitative size-exclusion chromatography (SEC) with multi-angle light scattering (SEC-MALS), we measured the αβ-tubulin binding stoichiometry for monomeric Alp14 (herein termed Alp14-monomer: residues 1-510), and dimeric Alp14 (herein termed wt-Alp14-dimer: residues 1-690) at 80-100 mM KCl ionic strength (Figure 1A-B, Figure 1D; details described in Figure 1 Supplement 1A-C, D-F; SEC-MALS control experiments shown in Figure 1 Supplement 2G-H; Table S2) (Al-Bassam et al., 2012). We show that 1 μM wt-Alp14-dimer binds four αβ-tubulins per dimer via its four TOG domains (dimeric TOG1-TOG2 arrays), whereas 1 μM wt-Alp14-monomer binds two αβ-tubulins per dimer via two TOG domains. Thus, TOG1 and TOG2 independently recruit αβ-tubulins (Figure 1A-B, D; Figure 1 Supplement 1A-C, D-F; Tables S1-S2).

Since TOG1 and TOG2 domains bind αβ-tubulins via narrow and mostly ionic binding interfaces, we studied the effect of a moderate increase in ionic strength (100-200 mM KCl) on αβ-tubulin binding capacities of TOG1 and TOG2 domains in these arrays (Ayaz et al., 2014; Ayaz et al., 2012). At 200 mM KCl, both 1 μM wt-Alp14-monomer and wt-Alp14-dimer bound roughly half as much αβ-tubulin than at 80-100 mM KCl. Thus, either TOG1 or TOG2 domains may lose part or all of their αβ-tubulin binding capacity at 200 mM KCl (Figure 1B, D; Figure 1

Supplement 1A-C, D-F and Tables S1-S2). These differences between the αβ-tubulin binding stoichiometries at 100 versus 200 mM KCl resolve discrepancies regarding Alp14- or Stu2-αβ-tubulin binding stoichiometries reported previously (Ayaz et al., 2014; Al-Bassam et al., 2012; Al-Bassam et al., 2006).

We next determined if the αβ-tubulin binding capacity of TOG1 or TOG2 changed within arrays due to a change in ionic strength from 100 to 200 mM KCl. Using SEC and SEC-MALs, we studied the αβ-tubulin binding stoichiometry for Alp14-dimer mutants in which either TOG1 (termed TOG1M) or TOG2 (termed TOG2M) were inactivated through multiple-residue mutations in the αβ-tubulin binding interfaces (Al-Bassam et al., 2007; Ayaz et al., 2012; see Materials and Methods; Figure 1C, Figure 1D; Figure 1 Supplement 1G-L). 1 μM TOG1M, which only includes two active TOG2 domains, bound two αβ-tubulins at 100 mM KCl, but almost completely dissociated from αβ-tubulin at 200 mM KCl. TOG1M and αβ-tubulin did not co-migrate on SEC, and most of the αβ-tubulin migrated as a separate peak at 200 mM KCl (Figure 1D, Figure 1 Supplement 1G-I; Tables S1-S2). In contrast, TOG2M, which only includes two active TOG1 domains, bound and co-migrated with αβ-tubulin in both 100 and 200 mM KCl conditions (Figure 1D, Figure 1 Supplement 1J-L, Tables S1-S2). Moreover, molar ratios of αβ-tubulin bound to TOG1M and TOG2M measured by quantitative-SEC at 100 mM KCl and maximal αβ-tubulin stoichiometry determined by SEC-MALS at 80 mM KCl were roughly half of that measured for wt-Alp14-dimer at 80-100 mM KCl (Figure 1C, D). These data support the independent and distinct affinities of TOG1 and TOG2 domains in recruiting αβ-tubulins while within either monomeric

or dimeric arrays, and that dimerization does not change the αβ-tubulin binding stoichiometry. TOG1 and TOG2 showed distinct αβ-tubulin binding behaviors at 100 and 200 mM KCl (Figure 1F; the SEC-MALS controls are shown in Figure 1 Supplement 2G)

Next, we quantitatively measured the absolute TOG1 and TOG2 binding affinities for αβ-tubulin using isothermal titration calorimetery (ITC), and determined how these affinities were influenced by changes in ionic strength at 100-200 mM KCl. ITC data showed that isolated TOG1 (residues 1-270) and TOG2 (residues 320-510) bound αβ-tubulins with roughly 2.5-fold difference in dissociation constants (Figure 1E; Figure 1 Supplement 3). At 100 mM KCl, the dissociation constants for TOG1 and TOG2 were measured at 70 and 173 nM, respectively. These data suggest that both TOG1 and TOG2 exhibit a moderately high affinity for αβ-tubulin with a 2.5-fold difference in affinity, nearly identical to that previously reported (Ayaz et al., 2014; Ayaz et al., 2012). However, at 200 mM KCl, we measured TOG1 and TOG2 αβ-tubulin dissociation constants at 1.5 μM and 3.2 μM, respectively, which showed 20-fold weaker affinity in absolute values compared to those measured at 100 mM KCl. Together, our studies suggest that within the cellular αβ-tubulin concentration range (5-10 μM) and 1 μM Alp14 at 100 mM KCl or below, each TOG1-TOG2 subunit tightly binds two αβ-tubulins, whereas at 200 mM KCl, each TOG1-TOG2 subunit binds one αβ-tubulin tightly via TOG1 and exchanges a second αβ-tubulin rapidly via TOG2. In conditions of 200 mM KCl, 1 μM Alp14, and 5-10 μM αβ-tubulin, TOG1 domains is almost completely occupied by αβ-tubulin while TOG2 domains is mostly dissociated

from αβ-tubulin (Figure 1F).

X-ray structures of a recruitment complex: pseudo-dimeric TOG1-TOG2 arrays in a head-to-tail square assembly that pre-orients αβ-tubulins

Our biochemical analyses suggest that structural studies of TOG array:αβ-tubulin complexes must be conducted at lower ionic strengths of 80-100 mM KCl and at high αβ-tubulin concentrations to avoid αβ-tubulin dissociation from TOG2 domains. To further increase TOG1-TOG2:αβ-tubulin complex formation and inhibit αβ-tubulin self-assembly under such conditions, we utilized the designed ankyrin repeat protein (DARPin) D1 (herein termed DRP), which specifically binds and neutralizes the β-tubulin polymerizing interface (Pecqueur et al., 2012). First, we studied if DRP binding to αβ-tubulin influenced wt-Alp14-monomer or wt-Alp14-dimer binding stoichiometries to multiple αβ-tubulins. We measured binding molar ratios using quantitative-SEC and stoichiometry using SEC-MALs for DRP-bound-αβ-tubulin to wt-Alp14-dimer and wt-Alp14-monomer in 80-100 mM KCl conditions, respectively (Figure 1A; Figure 1 Supplement 2A-F; Tables S1-S2). We showed that DRP did not affect the simultaneous binding of multiple αβ-tubulins to TOG1-TOG2 arrays in either wt-Alp14-monomer or wt-Alp14-dimer. 1 μM wt-Alp14-dimer formed a complex with four αβ-tubulins and four DRPs at a molar ratio of 2:4:4 (Figure 1D; Figure 1 Supplement 2D-F). We measured a mass of the wt-Alp14-monomer:αβ-tubulin:DRP complex by SEC-MALS that indicated a 1:2:2 stoichiometry complex in which each TOG1-TOG2 subunit bound two αβ-tubulins, each of which bound its own DRP (Figure 1A, D;

Figure 1 Supplement 2A-C, G; Table S1). The ability of Alp14-bound αβ-tubulin to bind stoichiometric amounts of DRP suggests that αβ-tubulins recruited by TOG arrays are in a non-polymerized state upon initial association with Alp14. This feature is consistent with a reported lack of cooperativity described between TOG1 and TOG2 in binding to αβ-tubulins (Ayaz et al., 2014). Thus, we used this strategy to identify crystallization conditions using TOG array orthologs from a variety of organisms (see Materials and Methods).

Crystals of the *Saccharomyces kluyveri* ortholog of Alp14 (herein termed sk-Alp14-monomer: residues 1-550) bound to αβ-tubulins and DRP grew in conditions similar to those used for SEC and SEC-MALS (Figure 2 Supplement 1A). Using crystals with either a native sk-Alp14-monomer or an sk-Alp14-monomer with a modified TOG1-TOG2 linker sequence (termed sk-Alp14-monomer-SL; see Materials and Methods; Figure 2 Supplement 2), we determined X-ray structures for 1:2:2 TOG1-TOG2 array:αβ-tubulin:DRP from complexes using sk-Alp14-monomer and sk-Alp14-monomer-SL using molecular replacement (see Materials and Methods) at 4.4-Å and 3.6-Å resolution, respectively (Table S3 and Figure 2 Supplement 1B, C). In the structures, TOG1 domains were clearly differentiated from TOG2 domains by their conserved C-terminal extension and jutting α-helix that were unambiguously identified in density-modified maps (Figure 2 Supplement 1D, E). Each asymmetric unit contained two wheel-shaped assemblies (Figure 2 Supplement 1F) representing two sets of alternating TOG1 and TOG2 domains oriented in a square-like conformation (termed the TOG square), with each TOG domain binding a DRP-

243 capped αβ-tubulin on its outer edge. Excluding the 10-residue TOG1-TOG2
244 linker region immediately preceding TOG2, the remaining 40 residues of the
245 linker were disordered (Figure 2 Supplement 1F-I).
246 The dimension of each wheel-like assembly was 210 x 198 x 60 Å (Figure 2A).
247 The 2:4:4 stoichiometry observed in the X-ray structure matched the
248 stoichiometry measured for wt-Alp14-dimer:αβ-tubulin:DRP complexes (Figure
249 1D; Figure 1 Supplement 2D-F). We hypothesized that sk-Alp14-monomer
250 formed dimeric organization, despite the lack of dimerization domains, due to the
251 high concentration of these complexes during crystallization. X-ray structures
252 revealed two TOG1-TOG2 subunits in a pseudo-dimeric assembly forming the
253 core of these complexes. In a TOG square, each TOG domain was bound to a
254 curved αβ-tubulin capped by a DRP through its outward-facing binding interface
255 and was not in contact with the neighboring TOG-bound αβ-tubulin (Figure 2A;
256 Figure 2 Supplement 1F-H). The distances and interaction patterns between
257 residues of α-tubulin and DRP bound to a neighboring β-tubulin indicated that
258 DRP only interacts with its cognate β-tubulin and does not bind a neighboring α-
259 tubulin (Figure 2 Supplement 1J, K). The latter suggests that DRP has no effect
260 on stabilizing each TOG square assembly. Rather, DRP binding only caps β-
261 tubulin, presenting a significant impediment to the polymerization of αβ-tubulins
262 while bound to the TOG1-TOG2 subunits. The αβ-tubulins bound to the TOG
263 square are positioned in a polarized orientation, due to the asymmetry in the
264 TOG domain αβ-tubulin interface and pseudo-dimeric TOG1-TOG2 subunit
265 interfaces within the TOG square (see below). The β-tubulin on a TOG1-bound

αβ-tubulin is rotated approximately 90° from its polymer-forming interface relative to the adjacent α-tubulin on a TOG2-bound αβ-tubulin (Figure 2B).

Two interfaces stabilize TOG1-TOG2 subunits into a TOG square assembly

The X-ray structures revealed that each TOG square is a dimer of TOG1-TOG2 array subunits assembled head-to-tail from alternating TOG1 and TOG2 domains. TOG domains were aligned along their narrow edges, analogous to four links attached head-to-tail forming an asymmetric square-like complex with two edges slightly longer than their orthogonal edges (Figure 2C, D). Two contact sites, which we term interfaces 1 and 2, stabilize the TOG square. These interfaces are formed by interactions formed via inter-HEAT repeat loops of each TOG domain, which are located on the opposite edges from the αβ-tubulin-binding sites. Although TOG1 and TOG2 domains are each 60-Å long, the TOG square assembly is slightly rectangular with 115-Å by 98-Å dimensions due to wider overlaps between TOG1 and TOG2 domains leading to 10-Å stagger at interface 1 sites, in contrast to the direct end-on corner-like interface 2 sites. Both interfaces 1 and 2 are stabilized by hydrophobic packing and ionic interaction zones (Figure 2E-H). Interface 1 packs a 668-Å^2 surface area and positions the TOG1 C-terminus at 90° to a 10-residue segment of the TOG1-TOG2 linker and the N-terminus of TOG2. The TOG1-TOG2 linker sequence forms an extended polypeptide that critically bridges interactions between TOG1 inter-HEAT repeat 6 α-helix/inter-HEAT 5-6 loop segment and the TOG2 inter-HEAT repeat 1-2/2-3 loop segments (Figure 2E, F). Interface 2 packs a 290-Å^2 surface area and

positions the TOG2 C-terminus at 90° to the N-terminus of TOG1 (Figure 2G, H). In interface 2, the TOG2 inter-HEAT repeat 4-5 loop interacts with the TOG1 inter-HEAT repeat 1-2/HEAT1 α-helix (Figure 2G). The residues forming interface 1 and interface 2 within TOG1, TOG2, and linker regions are either moderately or highly conserved (Figure 2F, H; Figure 2 Supplement 2). The total buried surface area stabilizing two sets of interfaces 1 and 2 in a TOG square is 1930 $Å^2$, which is moderate in size and dispersed for such a large assembly. This finding suggests that this conformation may be meta-stable and that DRP binding and its inhibition of αβ-tubulin polymerization may stabilize this intermediate.

Cysteine crosslinking and mass spectrometry reveal Alp14-dimer forms TOG square assembly interfaces in solution

Next we examined and chemically trapped the direct physical interactions between TOG1 and TOG2 interfaces observed in TOG square structures using cysteine mutagenesis and disulfide crosslinking. We generated mutants with specific cysteine pairs within the two sides of interface 1 (S180C, L304C) or interface 2 (S41C, E518C) in native dimeric sk-Alp14 (termed sk-Alp14-dimer; residues 1-724) (Figure 3A, B). We tested whether these interfaces formed inter-subunit contacts in dimeric TOG array by crosslinking via disulfide oxidation. A 110-kDa crosslinked species was observed in all conditions where soluble αβ-tubulin was added, and mass spectrometry (LC/MS-MS) confirmed that this intermediate was indeed a crosslinked α- and β-tubulin heterodimer (Figure 3C, D; Figure 3 Supplement 1A). We also observed a ~170-kDa species that

specifically formed in the αβ-tubulin-bound sk-Alp14 S180C-L304C mutant and not in the native sk-Alp14-dimer or the sk-Alp14-S41C-E518C mutants. Furthermore, this 170-kDa intermediate was also not observed with sk-Alp14-S180C-L304C without αβ-tubulin (Figure 3D). Mass spectrometry confirmed that this 170-kDa intermediate was indeed the sk-Alp14-S180C-L304C protein. Next, we mapped the cysteine residues involved in disulfide bonds in sk-Alp14-S180C-L304C mutants through peptide disulfide mapping after differential alkylation and mass spectrometry (see Materials and Methods). This approach revealed only two classes of peptides in sk-Alp14-S180C-L304C with 105 Da of mass added onto the cysteines, suggesting that they were engaged in disulfide bonds with the following sequence boundaries: 297-320 and 179-189 (Figure 3 Supplement 1B). These two peptide sequences represent TOG1 inter-HEAT-repeat and TOG1-TOG2 linker regions, both of which are involved in forming interface 1 in the X-ray structures (Figure 2). All of the remaining peptides with cysteine residues that were identified in sk-Alp14-S180C-L304C included 57 Da in added mass, suggesting that they were in the reduced form and did not form disulfide bridges. Thus, these data directly provide independent support of interface 1 of the TOG square conformation forming in sk-Alp14-dimer in solution outside of the crystallographic setting, and of indeed being the inter-subunit dimeric interface between two TOG-array subunits, as visualized in the crystal structures (Figure 3A, B).

Disrupting TOG square assembly interfaces destabilizes organization, but does not affect αβ-tubulin binding

We explored the role of interfaces 1 and 2 in stabilizing TOG square assembly and their effect on the αβ-tubulin capacity of TOG arrays. We generated three Alp14-dimer mutants that harbored either partially or fully disrupted interface 1 and 2 sites (Figure 4A-D). We targeted disruption of salt bridges or hydrophobic zones in interfaces 1 and 2 by mutating conserved alanines, leucines, or glutamates (Figure 2E,G; Figure 4A-D). Charged residues were either replaced with alanines or residues of the opposite charge, and hydrophobic residues were replaced with charged residues to dissociate hydrophobic interactions (Figure 4A-D). Initially, we disrupted interface 1 and 2 using one-, two-, or three-residue mutations in wt-Alp14-dimer. However, these mutants showed substantial levels of TOG square assemblies as assessed by negative stain electron microscopy (EM) (data not shown). Thus, we aimed to fully disrupt interfaces 1 and 2 by using seven to eight residues per interface. We mutated eight residues in wt-Alp14-dimer to disrupt interface 1 (termed INT1; Figure 4B), seven residues in wt-Alp14-dimer to disrupt interface 2 (termed INT2; Figure 4C), or fifteen residues to disrupt both interfaces 1 and 2 (termed INT1+2; Figure 4D) (see Materials and Methods).

We studied the αβ-tubulin binding capacities and stoichiometries of INT1, INT2, and INT1+2 compared to wt-Alp14-dimer using quantitative-SEC and SEC-MALS approaches, respectively, as described in Figure 1. INT1, INT2, and INT1+2

mutants bound nearly identical quantities of αβ-tubulin to wt-Alp14-dimer (Figure 4E; Figure 4F,G,H; Figure 4 Supplement 1). INT1, INT2, and INT1+2 bound approximately four αβ-tubulins at 80 mM KCl as assessed by SEC-MALS (Table S1,Table S2; Figure 4F,G,H,) and approximately half of the bound αβ-tubulin dissociated at 200 mM KCl as quantitated by quantitative-SEC (Figure 4D; Figure 4 Supplement 1 D,E,F).

We next used negative stain EM and 2D-single particle image analyses to compare the conformations of four αβ-tubulin-bound wt-Alp14-dimer assemblies to the αβ-tubulin:INT1, INT2 and INT1+2 mutant assemblies. Negative stain images showed that 4:2 wt-Alp14-dimer:αβ-tubulin complexes formed two types compact particle-like assemblies of either 15 or 19 nm diameter compact circular complexes (Figure 2) matched the general features previously described for yeast Stu2p-tubulin or Xmap215-tubulin we previously described (Al-Bassam et al., 2006; Brouhard et al., 2008). 2D-image class averages were compared via projection-matching to low resolution-filtered structural models for a TOG square with and without four αβ-tubulins, revealing TOG square bound to four αβ-tubulins matched well the density organization of the 19-nm diameter 2D-class averages (Figure 4I; Figure 4 supplement 2B). 2D-projections of a low resolution filtered TOG square model without αβ-tubulins bound matched well the organization of the 15 nm diameter class averages suggesting those classes represent TOG squares that likely lost their bound αβ-tubulins on the grid (Figure 4I; Figure 4 supplement 2C). These data provide another line of support that TOG array subunits form square assemblies in solution, and that they match the

organization of a TOG square bound to four αβ-tubulins (termed wheels) as observed in the crystal structure (Figure 2) or these dissociated from αβ-tubulin leading to isolated square-shaped assemblies (termed squares) (Figure 4). In contrast, INT1:αβ-tubulin complexes did not form square assemblies, and particles exhibited either open flexible organization with many inter-connected 8-nm long inter-connected densities or 16-nm long short filaments. 2D-image classification showed either 16-nm curved filaments, two 8-nm densities at right angles, or isolated 8-nm densities. 2D-projection matching using low resolution filtered models for single TOG1-TOG2 subunit bound to two αβ-tubulins from a TOG square structure, polymerized TOG-αβ-tubulin complexes (see next section), or with individual TOG-αβ-tubulin complexes (Ayaz et al, 2012) matched well to the three types of class averages (Figure 4J; Figure 4 supplement 2D-F). These data confirmed that these complexes were indeed either single TOG1-TOG2 subunits, with 90 degree pre-arranged and non-polymerized αβ-tubulin assemblies, TOG1-TOG2 bound to two polymerized αβ-tubulins assemblies, or disordered assemblies composed of isolated TOG-αβ-tubulin complexes. INT2-αβ-tubulin complexes showed similar pattern of class averages that matched similar models as INT1-αβ-tubulin complexes suggesting similarly dissociation of a single interface in the TOG square (Figure 4K; Figure 4 supplement 2G-I). While, INT1+2 αβ-tubulin complexes showed only dissociated, flexibly connected necklaces of 8-nm densities of αβ-tubulin (Figure 4L). 2D-image classification of these particles and 2D-projection matching of these complexes showed that each 8-nm class averages matched 2D-projections of a TOG-bound αβ-tubulin (Figure

4L; Figure 4 supplement 2J-K). Our biochemical and negative stain-EM analyses suggest that wt-Alp14 dimer TOG arrays form square-shaped assemblies that match the organization observed in the TOG square crystal structure. Specific aspects of TOG square organization are clearly disrupted leading to the predicted defects in organization in the INT1, INT2, and INT1+2 mutants without any effect on αβ-tubulin binding (Figure 4J,K,L). An interesting observation is that INT1 and INT2 mutants showed the propensity to form two polymerized αβ-tubulins filaments in some cases, suggesting that spontaneous in-solution αβ-tubulin polymerization occurs in the case of interface 1 and interface 2 destabilization (Figure 4J,K; Figure 4 supplement 2 E,H). The dual inactivation of both TOG square interfaces in INT1+2 resulted in dissociated TOG-αβ-tubulin complexes with a poor ability to form polymerize αβ-tubulins (Figure 4L; Figure 4 supplement 2).

X-ray structure of a polymerization complex: TOG1-TOG2 subunit unfurling promotes the concerted polymerization of two αβ-tubulin

The TOG square conformation shows how αβ-tubulins are recruited to TOG arrays but does not reveal how TOG arrays drive polymerization the recruited αβ-tubulins. We hypothesized that the TOG square structure may undergo a subsequent conformational change to promote polymerization of the recruited αβ-tubulins. To explore this transition, we created a biochemical approach to partially release αβ-tubulin from polymerization by relieving DRP inhibition of αβ-tubulin polymerization while they are bound to TOG arrays. We reasoned that a

structural transition may occur more readily if DRP dissociates from β-tubulin in a crystallization setting. We developed a strategy to conditionally release αβ-tubulin from polymerization while being recruited into TOG arrays by using a weakened affinity DRP. We reasoned that the increased dissociation of DRP may allow complexes to form polymerized αβ-tubulin intermediates in steady state, as seen in the negative stain studies. To accomplish this, we removed the N-terminal ankyrin repeat of DRP (herein termed DRPΔN). We measured DRPΔN affinity using ITC, revealing a three-fold decrease in its αβ-tubulin binding affinity as compared to DRP (Figure 5A-B). During purification, complexes of 1:2:2 sk-Alp14-monomer:αβ-tubulin:DRPΔN behaved similarly to those assembled with DRP on SEC (Figure 5C; Figure 5 Supplement 1). However, using crystallization conditions identical to those used to obtain the 4:4:2 TOG square conformation, we obtained crystals that exhibited a distinct rectangular morphology using sk-Alp14-monomer or sk-Alp14-dimer αβ-tubulin:DRPΔN complexes (see Materials and Methods; Figure 5 supplement 2A). These crystals formed in the same space group ($P2_1$) with distinct unit cell dimensions compared to the TOG square crystals (Table S3). These crystals exclusively formed only when DRPΔN was used with αβ-tubulin:sk-Alp14-monomer or -dimer complexes. We determined an X-ray structure to 3.3-Å resolution by molecular replacement using these crystals (Figure 5 Supplement 2B). The structure revealed a novel assembly consisting of complexes with the stoichiometry of 1:2 sk-Alp14-monomer:αβ-tubulin and a single DRPΔN positioned on the top end of TOG2-bound β-tubulin (termed the 1:2:1 structure;

Figure 5E, F; Figure 5 supplement 2C-D).

The refined 3.3-Å 1:2:1 X-ray structure revealed an extended conformation with two αβ-tubulins polymerized head-to-tail in a curved protofilament (Figure 5E-F). In this conformation, TOG1 and TOG2 did not form any interactions with each other and their adjoining linker became disordered (Figure 5E, F; Figure 5 Supplement 2C, D). TOG1 and TOG2 were specifically bound to the lower and upper αβ-tubulins, respectively, of a highly curved protofilament. Only a single DRPΔN capped the TOG2-bound αβ-tubulin (Figure 5E). Compared to the TOG square, this “unfurling” rearrangement required 68°-rotation and 32-Å translation of TOG2:αβ-tubulin hinging around interface 2 and TOG1-αβ-tubulin (Figure 6A, B). This transition promoted the concerted polymerization of TOG2:αβ-tubulin onto the plus-end of TOG1:αβ-tubulin, and consequently drove the dissociation of the second DRPΔN (Figure 5C, D). The two αβ-tubulin polymers in this complex were highly curved protofilaments (16.4° inter-dimer interface). This protofilament structure displayed ~3° more curvature than RB3/stathmin-αβ-tubulin curved protofilament structures (Table S5; Figure 5 Supplement 2E) (Nawrotek et al., 2011). Comparison of the αβ-tubulin dimer structure (α2β2) within this 1:2:1 structure to the unpolymerized αβ-tubulin structure revealed that polymerization is associated with a 5° rotation and 10-Å translation in the T7 loop and H8 helix of the TOG2-bound α-tubulin, which engages TOG1-bound β-tubulin elements and the E-site-bound GDP nucleotide (Figure 6C, D). The latter conformational change likely stabilizes inter-dimer αβ-tubulin interfaces (Figure

5D), burying a 1650-Å inter-dimer interface (Figure 5E, F). This conformational change occurs at a site similar to those observed during the MT lattice GTP hydrolysis transition (Alushin et al., 2014). Thus the 1:2:1 unfurled structure represents a concerted αβ-tubulin post-polymerization intermediate promoted by a single TOG1-TOG2 subunit prior to straightening the protofilament during polymerization at MT plus-ends.

Modeling αβ-tubulin bound TOG square and unfurled structure docking onto microtubule plus-ends

We next evaluated how X-ray structures of αβ-tubulin-bound TOG squares and unfurled TOG1-TOG2 αβ-tubulin assemblies can dock onto protofilament tips at MT plus-ends. Atomic models for these states were overlaid onto the terminal αβ-tubulins of curved GTP or GDP αβ-tubulin protofilament models (Figure 7). Attempts to dock the αβ-tubulin onto protofilament ends exposed at the MT minus-end caused substantial steric clashes, supporting the notion that TOG square states are completely incompatible with docking at MT minus-ends (data not shown). The four αβ-tubulin-bound TOG square assembly X-ray structure (Figure 2) was superimposed onto that of the terminal αβ-tubulin at protofilament ends in two docking orientations, either via the αβ-tubulins bound onto TOG1 or TOG2 (Figure 7A, B). We observed a slight steric surface overlap between the four αβ-tubulin-loaded TOG square and the curved protofilament when TOG1-αβ-tubulin was docked onto the β-tubulin at the protofilament plus-end (Figure 7A). This steric overlap was caused by overlap between αβ-tubulin-TOG2 from

the second TOG1-TOG2 subunit in the TOG square with penultimate αβ-tubulin from the protofilament end (Figure 7A; Figure 7 Supplement 1A). In contrast, we observed no steric contact when the TOG square was docked via αβ-tubulin-TOG2. In this orientation, the TOG1-αβ-tubulin from the second subunit was retracted by 10 Å from the penultimate αβ-tubulin in the protofilament in contrast to the TOG1-αβ-tubulin docking (Figure 7B). The differences between steric overlap of the TOG square with the protofilament in these two docking orientations were due to the asymmetric dimensions of the TOG square, caused by stagger between TOG1 and TOG2 domains at interface 1 compared to interface 2. These differences suggest that the destabilization of the TOG squares is more likely if TOG1-αβ-tubulin docks onto the protofilament plus-end in contrast to TOG2-αβ-tubulin docking. The unfurled 1:2 TOG1-TOG2:αβ-tubulin assembly can only be docked using TOG1-αβ-tubulin onto the protofilament plus-end and suggests that TOG2:αβ-tubulin is positioned the furthest away from the MT plus-end in this conformation. These models were used to assemble steps for a new MT polymerase model described in the discussion (Figure 8).

Discussion

A “Polarized Unfurling” model for TOG arrays as MT polymerases

Using the combination of structural and biochemical analyses, we propose a new model for TOG arrays as MT polymerases, which we term the “polarized-unfurling” model. The model is summarized in Figure 8 and animated in Video S1. This model is supported by X-ray structures of two states, negative EM

studies of αβ-tubulin complexes of wt-Alp14-dimer and three interface inactivated Alp14 mutants, differences in affinities of TOG1 and TOG2 domains for αβ-tubulins, and described via docking of models at protofilament ends at each step (Figure 7). Our model suggests that TOG arrays form two separate conformations that together promote MT polymerase activity: an αβ-tubulin recruitment complex as denoted by the TOG square (Figures 2-4) and an unfurled MT plus-end polymerization complex denoted by the polymerized 1:2:1 TOG1-TOG2: αβ-tubulin X-ray structures (Figure 5). We have effectively trapped these states by regulating the polymerization propensities for αβ-tubulins using DRP affinity while bound to TOG arrays (Figures 2 and 5). We hypothesize that the association of the αβ-tubulin-bound TOG square onto the MT plus-ends, via β-tubulin binding, drives the destabilization of the TOG square state and promotes the concerted unfurling of the TOG-αβ-tubulins to polymerize into a new protofilament.

The polarized unfurling MT polymerase cycle

We envision the polarized unfurling model as follow: 1) Upon recruiting four soluble αβ-tubulins, dimeric TOG1-TOG2 arrays in proteins such Alp14 or Stu2, organize into compact TOG square assemblies in solution (Figure 8A). These assemblies place αβ-tubulins in close proximity with each other in a near head-to-tail polarized while inhibiting spontaneous polymerization. This “ready-to-polymerize” orientation is due to the asymmetry in each TOG domain:αβ-tubulin interface and the unique head-to-tail assembly formed by two TOG1-TOG2 array

subunits formed in the TOG square (Figure 2). 2) The αβ-tubulin-loaded TOG square assemblies diffuse along the MT lattice, mediated by an interaction of the SK-rich regions immediately C-terminal to TOG2, with acidic tubulin C-termini exposed on MT surfaces (Figure 8A). Proximity of the SK-rich region to the TOG array is essential for MT polymerase activity, and increasing its polypeptide distance causes MT polymerase defects (Geyer et al., 2018; Al-Bassam et al., 2012; Brouhard et al., 2008). 3) When the αβ-tubulin loaded TOG squares reach the β-tubulins exposed at MT plus-end protofilament tips, α-tubulin of the TOG1- or TOG2-bound αβ-tubulin may polymerize with β-tubulin exposed at the MT plus-end tip (Figure 8B-I; Figure 2B). Although TOG squares may diffuse to MT minus-ends, docking onto α-tubulin at MT minus-ends is highly sterically inhibited, precluding the possibility of αβ-tubulin TOG square docking onto MT minus-ends. The αβ-tubulin docking of either TOG1 or TOG2 onto β-tubulin at MT plus-ends is likely to be random. However, two features of TOG domains favor TOG1-αβ-tubulin over TOG2 αβ-tubulin in docking onto MT plus-ends: A) TOG1 is more likely to be fully occupied by αβ-tubulin due to its slow exchange and high affinity compared to the rapid exchange of αβ-tubulin onto TOG2 (Figure 1). B) Steric overlap with MT protofilaments develops only if the TOG square docks via TOG1-αβ-tubulin but not if TOG2-αβ-tubulin docks (Figure 7; Figure 8A-I, 8B-I; Figure 7 Supplement 1A). Thus, TOG squares docking to protofilament ends via TOG1-αβ-tubulin destabilizes the TOG square in contrast with TOG2:αβ-tubulin, which will not destabilize the TOG square at protofilament tips, leading to selection of TOG1 at the docking site (Figurer 8B-II). 4) The MT

plus-end-induced TOG square destabilization likely triggers TOG square disassembly into two corner-shaped TOG1-TOG2 subunits at MT plus-ends. 5) Corner-like half-square TOG1-TOG2 subunit assemblies are then released which are likely unstable (Figure 8B-II), and interface 2 likely acts as a flexible hinge for TOG2 to freely rotate around TOG1, driven by Brownian motion. Reversible unfurling, or hinge rotation, promotes αβ-tubulin bound to TOG2 to polymerize catalytically onto the plus-end of the TOG1-bound αβ-tubulin (Figure 8B-III). The TOG1- and TOG2-bound αβ-tubulins polymerize in a single concerted unfurling event as seen in the polymerized TOG1-TOG2:αβ-tubulin X-ray structure (Figure 5E, F). This event effectively "unfurls" a single curved protofilament from two αβ-tubulins pre-oriented onto an αβ-tubulin loaded TOG1-TOG2 corner-like intermediate. No energy expenditure is required during unfurling, as reversible Brownian motion likely drives the unfurling activity. However, formation of the polymerized assembly intermediate is captured by the αβ-tubulin-αβ-tubulin inter-dimer polymerization interfaces, which become locked by the inter-dimer interface conformational change, as seen in in the polymerized state structure (Figure 6A, B). The αβ-tubulin inter-dimer interfaces (1650 $Å^2$ surface area in a single interface) may compete with TOG square reformation (1930 $Å^2$ in total for a TOG square). 6) A gradient in the αβ-tubulin exchange rates between TOG1 and TOG2 likely leads TOG2 to dissociate from its αβ-tubulin rapidly before TOG1 dissociates from its αβ-tubulin (Figure 1; Figure 8A-VI). The unfurled TOG1-TOG2 αβ-tubulin polymerized structure positions this affinity gradient spatially across lower and upper positions of the polymerized complex with

respect to the MT plus-end (Figure 6). A tightly bound αβ-tubulin on TOG1 likely anchors the TOG array onto the MT plus-end while the rapidly exchanging αβ-tubulin promotes TOG2 release- an intermediate that promotes accelerated MT polymerase (Figure 8B IV). 10) Protofilament straightening during MT plus-end closure likely induces TOG1 dissociation from the lower αβ-tubulin of the newly polymerized protofilament as suggested previously by the “catch and release” model (Ayaz et al 2012). The unbound TOG1-TOG2 arrays are finally released from the newly formed protofilament to reload with soluble αβ-tubulin from the cytoplasm. TOG arrays may then reform the TOG square assembly upon recruiting αβ-tubulins and restart the cycle, while the SK-rich region maintains contact with the polymerizing MT plus-end (Figure 8B-V) (Video S1).

Implications of “polarized unfurling”.

The polarized unfurling model suggests that the MT polymerase activity of TOG arrays is due to three features: 1) pre-organization of αβ-tubulins onto the TOG square. promoted by interfaces 1 and 2. 2) MT plus-end-induced unfurling of TOG square via TOG1-αβ-tubulin induced destabilization (Figure 7). 3) Reversible unfurling driven by Brownian motion and the polymerization capacity of αβ-tubulins being recruited TOG1-TOG2 squares disassemble. The propensity of TOG1-TOG2 subunit head-to-tail self-assembly is strongly enhanced by C-terminal coiled-coil-dimerization or the presence of TOG3-TOG4 in metazoan TOG arrays such as XMAP215/ch-TOG proteins. The positive charge of the SK-rich region is essential to associate with the MT surface. The polarized unfurling

611 model suggests that TOG1 and TOG2 serve specific roles in MT polymerase
612 activity, TOG1 anchors the array and destabilizes the TOG square organization
613 onto the MT plus-end, while TOG2 drives αβ-tubulin polymerization.
614
615 **Comparison to Other MT Polymerase Models**
616 Two other models were suggested for the functions of TOG arrays as MT
617 polymerases. In these models, TOG1 and TOG2 domains were suggested to
618 exhibit random or reversed orientations in the process of polymerizing αβ-tubulin,
619 compared to the polarized unfurling model (Ayaz et al., 2014; Fox et al., 2014).
620 Most recently, Geyer et al. (2018) studied the roles of TOG1 and TOG2 in MT
621 polymerase activity by generating All-TOG1 or All-TOG2 chimeras of the budding
622 yeast Stu2 MT polymerase. This study concluded that any two TOG domains,
623 regardless of identity, are required in a TOG array for MT polymerase activity.
624 This observation agrees with the importance of two adjacent TOG domains being
625 critical for forming a two αβ-tubulin polymerized complex. However, the study
626 concluded that no higher order of organization, such as the TOG square
627 observed here, was occurring since TOG domain identity did not influence MT
628 polymerase activity. However, our TOG square assembly structure indicates that
629 the critical 12-residue linker adjacent to TOG2 still remains in these All-TOG1 or
630 All-TOG2 Stu2 constructs. Thus, our studies demonstrate that the chimeric
631 constructs used in that study (Geyer et al 2018) still retained a substantial TOG
632 square assembly capacity, despite exchanging TOG1 for TOG2 domain
633 sequences. These chimeric Stu2 proteins were not structurally characterized in

that study, and thus their self-assembly properties using their modified TOG arrays remain unknown (Geyer et al 2018).

Our cysteine mutagenesis, crosslinking/mass spectrometry, and negative stain EM studies indicate wt-Alp14-dimer forms TOG squares upon binding αβ-tubulin in solution (Figure 3-4). Biochemical and negative stain-EM suggest that interfaces 1 & 2 organize TOG square assemblies, and that their inactivation in the INT1, INT2, and INT1+2 mutants results in specific loss of either interface 1 or interface 2 producing either single corner-like subunits bound to two orthogonally oriented αβ-tubulins, two spontaneously polymerized αβ-tubulins bound TOG1-TOG2 arrays (INT1 and INT2), or disorganized arrays composed of multiple TOG-αβ-tubulins (INT1+2); however these defects did not influence the ability of TOG arrays to bind αβ-tubulins. Our data support that interfaces 1 and 2 pre-orient αβ-tubulins and suggest that spontaneous polymerization may occur if interface 1 or interface 2 become destabilized, supporting our model (Figure 4-5). The polarized unfurling model explains a well-documented observation that could not be previously rationalized. Fusion of protein masses such as GFP protein, but not short tags, onto the TOG1 N-terminus severely inactivates MT polymerases, exclusively activating their MT depolymerase activity without affecting αβ-tubulin binding (Lechner et al., 2012 and references herein). Our model shows that N-terminal fusions on TOG arrays strongly interfere with formation of a TOG square by forming blocks that sterically hinder interface 2 formation.

Comparison to other MT regulatory proteins with TOG arrays

Other conserved classes of MT regulatory TOG-like array proteins, such as CLASP and Crescerin/CHE-12, may form similar TOG square-like particles and modulate MT dynamics in related mechanisms. For instance, the *S. pombe* CLASP:αβ-tubulin complexes form wheel-like particles with similar dimensions and promote local MT rescue (Al-Bassam and Chang, 2011; Al-Bassam et al., 2010; Das et al., 2015). However, the high-resolution organization of these different TOG arrays remains to be determined at high resolution.

Acknowledgments: We thank Dr. Julian Eskin (Brandeis University) for animating the microtubule polymerase mechanism. We thank Advanced Photon Source (APS) and Drs. K. Rajashankar, J. Schuermann, N. Sukumar, and D. Neau of the Northeastern Collaborative Access Team (NE-CAT) for use of the 24-IDC and IDE beam lines to collect all X-ray diffraction data for our crystallographic studies. We thank Dr. Christopher Fraser (UC Davis) for using his Nano-ITC. We thank Dr. Rick Mckenney (UC Davis), and Dr. Kevin Corbett (UC San Diego) for advice and critical reading of this manuscript. JAB and FC are supported by National Institutes of Health GM110283 and GM115185, respectively. This work is based upon research conducted at the NE-CAT beamlines, which are funded by the National Institute of General Medical Sciences from the National Institutes of Health (P41 GM103403). The Pilatus 6M detector on 24-ID-C beam line is funded by a NIH-ORIP HEI grant (S10 RR029205). The Eiger 16M detector on 24-ID-E beam line is funded by a NIH-ORIP HEI grant (S10OD021527). This research used resources of the Advanced Photon Source, a U.S. Department of Energy (DOE) Office of Science User Facility operated for the DOE Office of Science by Argonne National Laboratory under Contract No. DE-AC02-06CH11357. sk-Alp14-monomer:αβ-tubulin:DRP, sk-Alp14-monomer-SL:αβ-tubulin:DRP, and sk-Alp14-monomer:αβ-tubulin:DRPΔN are available at the protein data bank (PDB) under PDB-ID XXXX, PDB-ID XXXX and XXXX PDB-ID XXXX, respectively.

686 **Materials and Methods**

Reagent type (species) or resource	Designation	Source	Identifier	Additional information
Chemical compound, drug	Darpin D1 (Synthetic DNA)	Invitrogen	N/A	
Chemical compound, drug	GTP	Sigma	G-8877	
Chemical compound, drug	GDP	Sigma	G7127	
Chemical compound, drug	Crystallization plates	TTP Labtech	4150-05600	
Chemical compound, drug	Crystallization sparse matrix screens	Qiagen	N/A	
Chemical compound, drug	PEG-8000	Sigma	1546605	
Chemical compound, drug	PEG-2000	Sigma	8.21037	
Chemical compound, drug	Copper(II) sulfate	Sigma	C1297	
Chemical compound, drug	1, 10- phenanthroline	Sigma	131377	
Chemical compound, drug	Trypsin	Sigma	T6567	
Chemical compound, drug	Chymotrypsin	Sigma	C6423	
Chemical compound, drug	Iodoacetamide	Sigma	I6125	
Chemical compound, drug	4-Vinylpyridine	Sigma	V3204	
Other	2:4:4 sk-Alp14-550:αβ-Tubulin:DRP	Protein Data Bank	PDB: #6MZF	Deposited Data (Atomic coordinates)
Other	2:4:4 sk-Alp14-550-SL:αβ-Tubulin:DRP	Protein Data Bank	PDB: #6MZE	Deposited Data (Atomic coordinates)
Other	1:2:1 sk-Alp14-550: αβ-Tubulin:DRPΔN	Protein Data Bank	PDB: #6MZG	Deposited Data (Atomic coordinates)

Other	*Saccharomyces cerevisiae* Stu2p	UniprotKB/Swiss-Prot	P46675	Protein sequence
Other	*Saccharomyces kluyveri* Stu2p or Alp14p	Lachancea kluyveri NRRL Y-12651 chromosome	SKLU-Cont10078	Protein sequence
Other	*Schizosaccharomyces pombe* Alp14p	UniprotKB/Swiss-Prot	O94534	Protein sequence
Other	*Chaetomium thermophilum* Stu2	UniprotKB/Swiss-Prot	G0S3A7	Protein sequence
Other	SoluBL21 bacterial expression system	AmsBio	C700200	Model system (expression system)
Recombinant DNA reagent	pLIC_V2-*Sc* Stu2p-H_6	Current study	N/A	Recombinant DNA constructs Expressed in bacterial strains
Recombinant DNA reagent	pLIC_V2-*Sk* Stu2p-H_6	Current study	N/A	
Recombinant DNA reagent	pLIC_V2-Sc Stu2-550-H_6 (TOG1-TOG2 monomer)	Al-Bassam et al 2006		
Recombinant DNA reagent	pLIC_V2-KL-Stu2 -monomer-H_6 (residues 1-560)	Current study	NA	
Recombinant DNA reagent	pLIC_V2-CT Stu2-monomer-H_6 (residues 1-550)	Current study	NA	
Recombinant DNA reagent	pLIC_V2-SK Alp14-monomer-H_6 (residues 1-550)	Current study	N/A	

Recombinant DNA reagent	pLIC_V2-Sk Alp14-monomer-SL-H_6 (residues 1-550; linker residues replaced KL sequence; see methods)	Current study	N/A	
Recombinant DNA reagent	pLIC_V2-sk-wt-Alp14-dimer-H6 (residues 1-724)	Current study	N/A	
Recombinant DNA reagent	pLIC_V2-sk-Alp14-dimer-H_6	Current study	N/A	
Recombinant DNA reagent	S180C and L304C (residues 1-724)			
Recombinant DNA reagent	pLIC_V2-sk-Alp14-dimer-H_6	Current study	N/A	
Recombinant DNA reagent	S41C and E518C (residues 1-724)			
Recombinant DNA reagent	pLIC_V2-wt-Alp14-dimer-H_6 (residues 1-690)	Current study	N/A	
Recombinant DNA reagent	pLIC_V2-TOG1M - H_6 (residues 1-690: Y23A and R23A)	Current study	N/A	
Recombinant DNA reagent	pLIC_V2-TOG2M - H_6 (residues 1-690: Y300A and K381A)	Current study	N/A	
Recombinant DNA reagent	pLIC_V2-INT1-H_6 (residues 1-690: L206A, L208A, F275R D276A, L277A, V278A, K320L, R359A)	Current study	N/A	

Recombinant DNA reagent	pLIC_V2-INT2-H_6 (residues 1-690: L39D, S40A, D42A, L437D, S440A, E478A and R479A)	Current study	N/A	
Recombinant DNA reagent	pLIC_V2-INT1+2-H_6 (L206A, L208A, F275R D276A, L277A, V278A, K320L, R359A L39D, S40A, D42A, L437D, S440A, E478A and R479A)	Current study	N/A	
Recombinant DNA reagent	pET303-H_6-DRP	Current study	N/A	
Recombinant DNA reagent	pLIC_V2-H_6-DRPΔN	Current study	N/A	
Other	ab-tubulin purified from porcine brains	Current study	N/A	Native protein purification
Other	ab-tubulin purified from porcine brains	Castoldi and Popov, 2003		
Software, algorithm	ASTRA V6.0	Wyatt Technology	http://www.wyatt.com/products/software/astra.html	
Software, algorithm	NanoAnalyze	TA Instruments	http://www.tainstruments.com/	
Software, algorithm	EMAN2		http://blake.bcm.edu/emanwiki/EMAN2	
Software, algorithm	iMOSFLM	Battye et al., 2011	http://www.mrc-lmb.cam.ac.uk/harry/imosflm/ver721/quickguide.html	

Software, algorithm	PHASER	Terwilliger, 2000	http://www.phaser.cimr.cam.ac.uk/index.php/	
Software, algorithm	PHASER	McCoy et al., 2007	Phaser_Crystallographic_Software	
Software, algorithm	PyMol	Schro¨ dinger, LLC	http://www.pymol.org/	
Software, algorithm	UCSF-Chimera	Pattersen et al., 2004	https://www.cgl.ucsf.edu/chimera/	
Software, algorithm	DM from CCP4 suite	Cowtan, 1994	http://www.ccp4.ac.uk/html/dmmulti.html	
Software, algorithm	PHENIX	Adams et al., 2010	https://www.phenix-online.org	
Software, algorithm	anisotropy server	Strong et al., 2006	https://services.mbi.ucla.edu/anisoscale/	
Software, algorithm	Phyre protein homology model	Kelley et al., 2015	www.sbg.bio.ic.ac.uk/phyre2/html/page.cgi?id=index	
Software, algorithm	Cr-yolo	Wagner et al., 2018	http://sphire.mpg.de/wiki/	
Software, algorithm	Relion 2.2	Kimanius et al., 2016	https://www2.mrc-lmb.cam.ac.uk/relion/index.php	
Software, algorithm	Cryosparc	Punjani et al.,2017	https://cryosparc.com/	
Software, algorithm	MolProbity	Chen et al., 2010	http://molprobity.biochem.duke.edu	

Software, algorithm	Coot	Emsley et al., 2010	http://www2.mrc-lmb.cam.ac.uk/personal/pemsley/coot/	
Software, algorithm	BLENDER 3D-animation	Blender foundation	https://www.blender.org/	

687

Protein expression and purification of Alp14 and sk-Alp14 proteins

The coding regions for MT polymerases from *Schizosaccharomyces pombe* Alp14p (accession: BAA84527.1), *Saccharomyces cerevisiae* Stu2p (accession: CAA97574.1), *Saccharomyces kluyveri* Alp14 or Stu2p (coding region identified in accession: SKLU-Cont10078), and *Chaetomium thermophilum* Stu2p (accession: XP_006692509) were inserted into bacterial expression vectors with a C-terminal His-tag. wt-Alp14-monomer (residues 1-510), wt-Alp14-dimer (residues 1-690), sk-Alp14-monomer (residues 1-550), sk-Alp14-dimer (residues 1-724), Sc-Stu2-dimer (residues 1-746), and Ct-Stu2-dimer (residues 1-719) constructs were generated, including with or without the SK-rich and coiled-coil dimerization regions. TOG1M and TOG2M mutants were generated via point mutagenesis of Y23A and R23A to inactivate TOG1 domains (TOG1M); and Y300A and K381A to inactivate TOG2 domains (TOG2M) (Al-Bassam et al., 2012). The INT1+2 mutant was generated via gene synthesis (Epoch Life Science) by introducing 15-residue mutations into the wt-Alp14-dimer sequence (L206A L208A F275R D276A L277A V278A K320L R359A L39D S40A D42A L437D S440A E478A R479A). The INT1 and INT2 mutants were generated by a PCR swapping strategy of INT1+2 with wt-Alp14-dimer leading to INT1 with 8-residue mutations (L206A L208A F275R D276A L277A V278A K320L R359A) and INT2 with 7-residue mutations (L39D S40A D42A L437D S440A E478A R479A). Generally, constructs were transformed and expressed in BL21 bacterial strains using the T7 expression system, and were grown at 37 °C and induced with 0.5 mM isopropyl thio-β-glycoside at 18 °C overnight. Cells were centrifuged

and then lysed using a microfluidizer (Avastin). Extracts were clarified via centrifugation at 18,000 x *g*. Proteins were purified using Ni-IDA (Macherey-Nagel) and/or ion exchange using Hitrap-SP or Hitrap-Q chromatography followed by size exclusion chromatography using a Superdex 200 (30/1000) column (GE Healthcare). DRP was synthesized (Gene Art, Life Technologies), inserted into bacterial expression vectors with a C-terminal 6×His tag, and expressed as described above. Proteins were purified using Ni-NTA (Macherey-Nagel) followed by Hitrap Q ion exchange and followed by size exclusion chromatography as described above. Purified proteins were used immediately or frozen in liquid nitrogen for future use.

Biochemical analyses of Alp14:αβ-tubulin complexes

Soluble porcine αβ-tubulin (10 μM or 20 μM) purified using two GTP-polymerization cycles at high ionic strength as previously described (Castoldi and Popov, 2003) was mixed with 5 μM *S. kluyveri* (sk) or *S. pombe* wt-Alp14-monomer, wt-Alp14-dimer, TOG1M, TOG2M, INT1, INT2, or INT1+2 mutant proteins and then diluted 5-fold. To assess αβ-tubulin assembly, the protein mixtures were analyzed by mixing the proteins into 0.5-mL volumes and injecting them into a Superdex 200 (10/300) size exclusion chromatography (SEC) column equilibrated in 100 mM or 200 mM KCl binding buffer (50 mM HEPES [pH 7.0], 1 mM $MgCl_2$, and 1 mM β-mercaptoethanol with 100 mM KCl or 200 mM KCl) using an AKTA purifier system (GE Healthcare). Elution fractions (0.5 mL) were collected and analyzed via sodium dodecyl sulfate polyacrylamide gel

electrophoresis (Bio-Rad). The αβ-tubulin- and Alp14-containing bands were quantitated using densitometry to determine the amounts of bound and unbound αβ-tubulin in each SEC fraction. Molecular masses of wt-Alp14-monomer, wt-Alp14-dimer, TOG1M, TOG2M, INT1, INT2, and INT1+2 proteins, αβ-tubulin, and their complexes were measured using SEC-coupled multi-angle light scattering (SEC-MALS). Complexes were separated on Superdex 200 SEC columns (GE Healthcare) while measuring UV absorbance (Agilent 1100-Series HPLC), light scattering (Wyatt Technology miniDAWN TREOS), and refractive index (Wyatt Technology Optilab T-rEX). Concentration-weighted molecular masses for each peak were calculated using ASTRA 6 software (Wyatt Technology).

Isothermal titration calorimetery (ITC) was performed using a Nano-ITC (TA Instruments) to determine DRP and DRPΔN affinities for αβ-tubulin. Experiments were performed at 25 °C. Soluble αβ-tubulin, DRP, and DRPΔN were diluted in 50 mM HEPES buffer, pH 7.3, 100 mM KCl, 1 mM $MgCl_2$, and 50 μM GDP. The sample cell was filled with tubulin (20-40 μM) for every experiment. 135-250 μM of DRP or DRPΔN solutions were injected in volumes of 2 or 5 μL in a series of controlled doses into the sample cell. To determine TOG1 and TOG2 affinities for αβ-tubulin with DRP, proteins were diluted in 50 mM HEPES buffer, pH 7.3, 100 or 200 mM KCl, and 1 mM MgCl2. 100-250 μM of TOG1 or TOG2 solutions were injected in volumes of 2 or 5 μL in a series of controlled does into the sample cell containing 1:1 molar ratio of αβ-tubulin and DRP (20-40 μM). The results were analyzed with NanoAnalyze software (TA Instruments). Thermodynamic parameters were calculated using the standard thermodynamic equation:

757 $-RT\ln K_a = \Delta G = \Delta H - T\Delta S$, where ΔG, ΔH, and ΔS are the changes in free
758 energy, enthalpy, and entropy of binding, respectively, T is the absolute
759 temperature, and R is the gas constant (1.98 cal mol^{-1} K^{-1}).
760
761 **Crystallization of sk-Alp14:αβ-tubulin:DRP or DRPΔN complexes**
762 Complexes (200 μM) were screened for crystallization using commercial sparse
763 matrix (Qiagen) or homemade screens in 96-well format using a Mosquito robot
764 (TTP Labtech) via the hanging drop method. Cube-shaped crystals (5 μm on
765 each edge) formed for sk-Alp14-monomer:αβ-tubulin:DRP complexes and grew
766 over 4-7 days in 50 mM PIPES, 100 mM $MgCl_2$ [pH 7.0], and 10-15% PEG-8000.
767 Larger crystals were grown using micro-seeding (Figure 2-Supplement 2A). To
768 obtain improved X-ray diffraction (see below), we used an sk-Alp14-monomer
769 construct in which non-conserved 256-297 residue linkers were replaced by the
770 shorter linker (including the residue sequence -
771 AVPAQSDNNSTLQTDKDGDTLMGN-) from the *K. lactis* ortholog sequence
772 (termed sk-Alp14-monomer-SL). Crystals were transferred to 50 mM PIPES, 100
773 mM $MgCl_2$ [pH 7.0], 15% PEG-8000, and 25% glycerol for cryo-protection and
774 flash frozen in liquid nitrogen.
775 Rectangular crystals of sk-Alp14-monomer:αβ-tubulin:DRPΔN complexes formed
776 in 7-10 days under the same conditions described for cube-shaped TOG1-
777 TOG2:αβ-tubulin:DRP crystals. These rectangular crystals exclusively formed
778 using DRPΔN (did not form with DRP), and were obtained using a variety of
779 constructs of monomeric as well as dimeric sk-Alp14-monomer (Table S3).

Rectangular sk-Alp14-monomer:αβ-tubulin:DRPΔN crystals were treated for cryo-protection and flash frozen as described above.

X-ray diffraction and structure determination of sk-Alp14:αβ-tubulin assemblies

More than 100 sk-Alp14-monomer:αβ-tubulin:DRP crystals were screened for X-ray diffraction at the Argonne National Laboratory at the Advanced Photon Source microfocus 24-ID-C beamline. Anisotropic X-ray diffraction data were collected for the best cube-shaped crystals in the $P2_1$ space group to 4.4-Å resolution in the best dimension, with unit cell dimensions *a*=219 Å, *b*=108 Å, and *c*=283 Å (Figure 2 Supplement 1). The sk-Alp14-monomer-SL:αβ-tubulin:DRP crystals showed improved diffraction and decreased anisotropy to 3.6-Å resolution in an identical $P2_1$ unit cell (Table S3). X-ray diffraction data were indexed and scaled using iMOSFLM and treated for anisotropic diffraction using ellipsoidal truncation on the UCLA diffraction anisotropy server (services.mbi.ucla.edu/anisoscale). Phase information was determined using TOG1 (PDB ID:4FFB), TOG2 (PDB ID:4U3J), αβ-tubulin dimer, and DRP (PDB ID:4DRX) models using molecular replacement. Briefly, a truncated poly-alanine TOG domain including only its HEAT repeats was used in the molecular replacement rotation and translation search (Figure 2 Supplement 1B-C). Eight αβ-tubulin and TOG domain solutions were identified based on the Log Likelihood Gain (LLG) values (Figure 2 Supplement 1B-C). After eight cycles of density modification, the electron density map revealed the TOG1 domains

exclusively due to the unique C-terminal linker and vertical helix densities (Figure 2 Supplement 1D-E). Density for eight DRP molecules was identified and built. DRP molecules interacted only with their cognate β-tubulin and did not form interfaces with α-tubulin from neighboring molecules (Figure 2 Supplement 1H). Two 2:4:4 sk-Alp14-monomer:αβ-tubulin:DRP wheel-like models were built and subjected to cycles of rigid-body refinement and model building using the *S. kluyveri* ortholog sequence. Each asymmetric unit contained two wheel-like assemblies (Figure 2 Supplement 1E). TOG1-TOG2 linker residues (residues 265-299 in native sk-Alp14 and residues 260-277 in sk-Alp14-SL) were not observed and were presumed to be disordered (Figure 2 Supplement 1F-H). Density maps from each of the wheel-like models were averaged using non-crystallographic symmetry and then refined using the PHENIX program (Adams et al., 2010). Initially, models were refined using non-crystallographic symmetry (16 fold NCS) restraints and strictly constrained coordinates with group B-factor schemes. In the final stage refinement, the strategy was switched to individual positional and isotropic B-factor with automatic weight optimization. A 4.4-Å sk-Alp14-monomer:αβ-tubulin:DRP structure and 3.6-Å sk-Alp14-monomer-SL:αβ-tubulin:DRP structure are reported; refinement statistics appear in Table S3.

Rectangular crystals formed from sk-Alp14-monomer:αβ-tubulin: DRPΔN diffracted to 3.3-Å resolution at the Argonne National Laboratory at the Advanced Photon Source microfocus APS 24-IDC beamline. X-ray diffraction data were indexed in the $P2_1$ space group with unique unit cell dimensions *a*=115 Å, *b*=194 Å, and *c*=149 Å, with two complexes in each unit cell (table S3). Phase

information was determined using molecular replacement using the TOG1 and TOG2 domains and curved αβ-tubulin as search models (Figure 5 Supplement 1B). TOG1 and TOG2 domains were identified after cycles of density modification as described above. Four αβ-tubulins, four TOG domains, and two DRPΔN models were placed in the unit cell. The identity of TOG domains was determined using the conserved C-terminal linker and jutting helix in the TOG1 domain sequence. A single DRPΔN molecule was identified bound per two αβ-tubulin polymerized complex. Data from each extended assembly were combined using non-crystallographic symmetry (8-fold NCS) and were averaged and refined using the program PHENIX (Adams et al., 2010) (Table S3). The individual positional coordinates and isotropic B-factor were refined with automatic weight optimization in the final stage. A 3.3-Å resolution refined density map is presented in Figure 5 Supplement 1C. Examining data quality of sk-Alp14-monomer:αβ-tubulin:DRP or sk-Alp14-monomer:αβ-tubulin:DRPΔN using PHENIX (Adams et al., 2010) indicated that the diffraction data contained a small degree of pseudo-merohedral twinning. The twin fractions were adjusted during refinement of both models.

Cysteine mutagenesis and crosslinking analyses of sk-Alp14:αβ-tubulin assemblies

Based on the sk-Alp14-monomer:αβ-tubulin:DRP crystal structure, the *S. kluyveri* ortholog protein sk-Alp14, in its dimer form (residues 1-724), was used to generate crosslinking mutations. Interface 1 residues, which are in close

proximity to each other, were mutated to cysteine: Ser180Cys (S180C) and Leu304Cys (L304C), which we termed S180C-L304C. Interface 2 residues, which are in close proximity to each other, were also mutated to cysteine: Ser41Cys (S41C) and Glu518Cys (E518C), which we termed S41C-E518C. The *S. kluyveri* ortholog dimer S180C-L304C mutant and S41C-E518C mutant proteins were purified as described above (Figure 3E). These constructs were used either directly or to make complexes with αβ-tubulin in a 2:4 (subunit:αβ-tubulin) molar ratio, as described in Figure 1A. These S180C-L304C and S41C E518C mutants or their αβ-tubulin complexes were then treated using 5 mM Cu-phenanthroline in 50 mM HEPES and 100 mM KCl, pH 7.0, for 5 min, then treated with 5 mM EDTA. These protein mixtures were subjected to SDS-PAGE under oxidizing conditions.

For LC/MS-MS mass spectrometry-based disulfide peptide mapping, S180C-L304C sk-Alp14 oxidized SDS-PAGE bands were subjected to in-gel proteolysis using either trypsin or chymotrypsin. Fragmented peptides were then purified and treated with 5 mM iodioacetamide, which covalently adds 57-Da in mass onto reduced cysteine-containing peptides, and does not affect cysteines locked in disulfides. The peptide mixture was then treated with 5 mM dithiothriatol to reduce disulfides and then treated with 5-vinyl chloride, which covalently adds 105-Da mass units onto newly reduced cysteine-containing peptides. LCMS/MS mass spectrometry was performed and the resulting peptides were analyzed. Peptides covering 90% of sk-Alp14 were identified as were the majority of

cysteines. Only two peptides were identified with cysteine residues that included 105-Da mass units added as described in Figure 4, S6D.

Negative stain electron microscopy and image analysis of wt-Alp14 and TOG inactivated mutants in complex with αβ-tubulins

SEC-purified αβ-tubulin complexes of wt-Alp14-dimer, INT1, INT2, and INT1+2 at 100 mM KCl supplemented with glutaraldehyde 0.05% and 4:2 molar ratio were placed on glow discharged grids, blotted after 30-60 seconds, and then stained with multiple washes of 0.1% uranyl formate at pH 7. All the images for negatively stained specimens were grids were collected on an electron microscope (JEM-2100F; JEOL) equipped with a field emission gun using low-dose mode at 200 KeV paired with a DE-20 direct electron detector device (DDD) operating in integration mode. The images were then processed using neural networks picking using Cr-YOLO (Wagner et al, https://doi.org/10.1101/356584). The particle coordinates were imported into relion 2.2. Images were CTF corrected using CTFFIND4 (Grant et al,). Particles were manually screened and subjected to rounds of 2D-classification either in Relion 2.2 or using Cryosparc (Punjani et al 2017; Kimanius et al 2016). For each data set, 2D-Class averages were grouped based on their conformation then compared to 30 Å resolution filtered models of 4:2 αβ-tubulin: TOG2-TOG2 in square conformation (Figure 2) and single TOG1-TOG2 subunit from the square conformation in the bent conformation bound to two non-polymerized αβ-tubulins (Figure 6), TOG1-TOG2 in the polymerized conformation (Figure 5) and a single TOG domain bound αβ-

tubulin (PDB-ID:4FFD). The projection matching was performed using EMAN2 command e2classvsproj.py at 1-5 angular degree increments (Tang et al, 2007).

Animating the MT polymerase "polarized unfurling" mechanism

The animation was created using BLENDER 3D-animation software (http://blender.org) as follows. Briefly, surface and ribbon models of PDB coordinates representing the structures were exported from UCSF-Chimera and imported into BLENDER, and then smoothed and optimized to generate animated models. Additional protein SK-rich regions and coiled-coil domains, whose structures are unknown, were thus modeled using sequence length and other information as guidance. The microtubule lattice was modeled based on the tubulin structure (PDB ID 36JF). The dissociation of TOG1 and TOG2 domains from αβ-tubulins were simulated in the animation, based on biochemical studies described in Figure 1 and its figure supplements.

References

Adams, P.D., Afonine, P.V., Bunkoczi, G., Chen, V.B., Davis, I.W., Echols, N., Headd, J.J., Hung, L.W., Kapral, G.J., Grosse-Kunstleve, R.W.*, et al.* (2010). PHENIX: a comprehensive Python-based system for macromolecular structure solution. Acta Crystallogr D Biol Crystallogr *66*, 213-221.

Akhmanova, A., and Steinmetz, M.O. (2008). Tracking the ends: a dynamic protein network controls the fate of microtubule tips. Nat Rev Mol Cell Biol *9*, 309-322.

Akhmanova, A., and Steinmetz, M.O. (2011). Microtubule End Binding: EBs Sense the Guanine Nucleotide State. Curr Biol *21*, R283-285.

Akhmanova, A., and Steinmetz, M.O. (2015). Control of microtubule organization and dynamics: two ends in the limelight. Nat Rev Mol Cell Biol.

Al-Bassam, J. (2014). Reconstituting dynamic microtubule polymerization regulation by TOG domain proteins. Methods Enzymol *540*, 131-148.

Al-Bassam, J., and Chang, F. (2011). Regulation of microtubule dynamics by TOG-domain proteins XMAP215/Dis1 and CLASP. Trends Cell Biol *21*, 604-614.

Al-Bassam, J., Kim, H., Brouhard, G., van Oijen, A., Harrison, S.C., and Chang, F. (2010). CLASP promotes microtubule rescue by recruiting tubulin dimers to the microtubule. Dev Cell *19*, 245-258.

Al-Bassam, J., Kim, H., Flor-Parra, I., Lal, N., Velji, H., and Chang, F. (2012). Fission yeast Alp14 is a dose-dependent plus end-tracking microtubule polymerase. Mol Biol Cell *23*, 2878-2890.

Al-Bassam, J., Larsen, N.A., Hyman, A.A., and Harrison, S.C. (2007). Crystal structure of a TOG domain: conserved features of XMAP215/Dis1-family TOG domains and implications for tubulin binding. Structure *15*, 355-362.

Al-Bassam, J., van Breugel, M., Harrison, S.C., and Hyman, A. (2006). Stu2p binds tubulin and undergoes an open-to-closed conformational change. J Cell Biol *172*, 1009-1022.

Alushin, G.M., Lander, G.C., Kellogg, E.H., Zhang, R., Baker, D., and Nogales, E. (2014). High-resolution microtubule structures reveal the structural transitions in alphabeta-tubulin upon GTP hydrolysis. Cell *157*, 1117-1129.

Ayaz, P., Munyoki, S., Geyer, E.A., Piedra, F.A., Vu, E.S., Bromberg, R., Otwinowski, Z., Grishin, N.V., Brautigam, C.A., and Rice, L.M. (2014). A tethered delivery mechanism explains the catalytic action of a microtubule polymerase. Elife *3*, e03069.

Ayaz, P., Ye, X., Huddleston, P., Brautigam, C.A., and Rice, L.M. (2012). A TOG:alphabeta-tubulin complex structure reveals conformation-based mechanisms for a microtubule polymerase. Science *337*, 857-860.

945 Bieling, P., Telley, I.A., Hentrich, C., Piehler, J., and Surrey, T. (2010). Fluorescence
946 microscopy assays on chemically functionalized surfaces for quantitative imaging of
947 microtubule, motor, and +TIP dynamics. Methods Cell Biol *95*, 555-580.

948 Brouhard, G.J., and Rice, L.M. (2014). The contribution of alphabeta-tubulin curvature to
949 microtubule dynamics. J Cell Biol *207*, 323-334.

950 Brouhard, G.J., Stear, J.H., Noetzel, T.L., Al-Bassam, J., Kinoshita, K., Harrison, S.C.,
951 Howard, J., and Hyman, A.A. (2008). XMAP215 is a processive microtubule polymerase.
952 Cell *132*, 79-88.

953 Castoldi, M., and Popov, A.V. (2003). Purification of brain tubulin through two cycles of
954 polymerization-depolymerization in a high-molarity buffer. Protein Expr Purif *32*, 83-88.

955 Cullen, C.F., Deak, P., Glover, D.M., and Ohkura, H. (1999). mini spindles: A gene
956 encoding a conserved microtubule-associated protein required for the integrity of the
957 mitotic spindle in Drosophila. J Cell Biol *146*, 1005-1018.

958 Das, A., Dickinson, D.J., Wood, C.C., Goldstein, B., and Slep, K.C. (2015). Crescerin
959 uses a TOG domain array to regulate microtubules in the primary cilium. Mol Biol Cell *26*,
960 4248-4264.

961 Fox, J.C., Howard, A.E., Currie, J.D., Rogers, S.L., and Slep, K.C. (2014). The
962 XMAP215 family drives microtubule polymerization using a structurally diverse TOG
963 array. Mol Biol Cell *25*, 2375-2392.

964 Geyer E.A., Miller M.P., Brautigam C.A., Biggins S., Rice L.M. (2018). Design principles
965 of a microtubule polymerase. Elife. pii: e34574. doi: 10.7554/eLife.34574.

966 Howard, A.E., Fox, J.C., and Slep, K.C. (2015). Drosophila melanogaster mini spindles
967 TOG3 utilizes unique structural elements to promote domain stability and maintain a
968 TOG1- and TOG2-like tubulin-binding surface. J Biol Chem *290*, 10149-10162.

969 Kimanius D, Forsberg BO, Scheres SH, Lindahl E. Accelerated cryo-EM structure
970 determination with parallelisation using GPUs in RELION-2. (2016) Elife, 15;5.
971 pii: e18722. doi: 10.7554/eLife.18722.

972 Lechner, B., Rashbrooke, M.C., Collings, D.A., Eng, R.C., Kawamura, E., Whittington,
973 A.T., and Wasteneys, G.O. (2012). The N-terminal TOG domain of Arabidopsis MOR1
974 modulates affinity for microtubule polymers. J Cell Sci *125*, 4812-4821.

975 Maurer, S.P., Cade, N.I., Bohner, G., Gustafsson, N., Boutant, E., and Surrey, T. (2014).
976 EB1 accelerates two conformational transitions important for microtubule maturation and
977 dynamics. Curr Biol *24*, 372-384.

978 Miller, M.P., Asbury, C.L., and Biggins, S. (2016). A TOG Protein Confers Tension
979 Sensitivity to Kinetochore-Microtubule Attachments. Cell *165*, 1428-1439.

980 Nawrotek, A., Knossow, M., and Gigant, B. (2011). The determinants that govern
981 microtubule assembly from the atomic structure of GTP-tubulin. J Mol Biol *412*, 35-42.

Pecqueur, L., Duellberg, C., Dreier, B., Jiang, Q., Wang, C., Pluckthun, A., Surrey, T., Gigant, B., and Knossow, M. (2012). A designed ankyrin repeat protein selected to bind to tubulin caps the microtubule plus end. Proc Natl Acad Sci U S A *109*, 12011-12016.

Punjani A, Rubinstein JL, Fleet DJ, Brubaker MA. cryoSPARC: algorithms for rapid unsupervised cryo-EM structure determination (2017) Nat Methods, 14:290-296.

Reber, S.B., Baumgart, J., Widlund, P.O., Pozniakovsky, A., Howard, J., Hyman, A.A., and Julicher, F. (2013). XMAP215 activity sets spindle length by controlling the total mass of spindle microtubules. Nat Cell Biol *15*, 1116-1122.

Slep, K.C., and Vale, R.D. (2007). Structural basis of microtubule plus end tracking by XMAP215, CLIP-170, and EB1. Mol Cell *27*, 976-991.

Tanaka, K., Mukae, N., Dewar, H., van Breugel, M., James, E.K., Prescott, A.R., Antony, C., and Tanaka, T.U. (2005). Molecular mechanisms of kinetochore capture by spindle microtubules. Nature *434*, 987-994.

Tang G, Peng L, Baldwin PR, Mann DS, Jiang W, Rees I, Ludtke SJ. EMAN2: an extensible image processing suite for electron microscopy (2007) J Struct Biol., 157(1):38-46.

Wang, P.J., and Huffaker, T.C. (1997). Stu2p: A microtubule-binding protein that is an essential component of the yeast spindle pole body. J Cell Biol *139*, 1271-1280.

Widlund, P.O., Stear, J.H., Pozniakovsky, A., Zanic, M., Reber, S., Brouhard, G.J., Hyman, A.A., and Howard, J. (2011). XMAP215 polymerase activity is built by combining multiple tubulin-binding TOG domains and a basic lattice-binding region. Proc Natl Acad Sci U S A *108*, 2741-2746.

Figure Legends

Figure 1. TOG1 and TOG2 domains bind αβ-tubulins and exchange them at different rates, **within Alp14 TOG arrays.** (A) Top, domain organization of Alp14-monomer. Bottom, SEC-MALs for wt-Alp14-monomer at 100 mM KCl with and without DRP, revealing two αβ-tubulins bound in a non-polymerized state. (B) Top, domain organization of Alp14-dimer. Bottom, SEC-MAL for wt-Alp14-dimer in αβ-tubulin complex at 2:4 stoichiometry at 100 mM and 200 mM KCl, revealing that four αβ-tubulins bind dimeric-Alp14 with four TOG domains and two αβ-tubulins dissociate upon increase of ionic strength (masses reported in Table 1). (C) Top, organization of TOG-inactivated Alp14-dimer (C: TOG1M, TOG2M). Bottom, SEC-MALS of 4:2 TOG1M- and TOG2M-αβ-tubulin at 100 mM KCl revealing half of the αβ-tubulin binding stoichiometry compared to wt-Alp14-dimer (shown in B). (D) SEC-based titration measured through analyses of masses from SDS-PAGE (Table S2; Materials and Methods) of Alp14-monomer, Alp14-dimer, and TOG1M and TOG2M with and without DRP binding, reveals the binding capacities of TOG1 and TOG2 domains in these constructs and their non-equivalence in αβ-tubulin exchange at 200 mM KCl. DRP binding to αβ-tubulin does not influence αβ-tubulin binding to TOG arrays. Details are described in Figure 1 Supplement 1-2. (E) Isothermal titration calorimetery (ITC) reveals TOG1 and TOG2 exchange αβ-tubulin with non-equivalent rates at 200 mM KCl. At 100 mM KCl, TOG1 and TOG2 both slowly dissociate from αβ-tubulin with K_D=70 nM and K_D=173 nM, respectively. At 200 mM KCl, TOG1 dissociates from αβ-tubulin slowly with a K_D =1.50 μM while TOG2 mostly

dissociates from αβ-tubulin with a K_D=3.25 μM. ITC binding curves are shown in Figure 1 Supplement 3. (F) Model for non-equivalent activities of TOG1 and TOG2 within TOG array for recruiting αβ-tubulins.

Figure 2. X-ray structures reveal αβ-tubulins bound in a wheel-like organization around a pseudo-dimeric TOG square complex. (A-B) 3.6-Å X-ray crystal structure of the *S. kluyveri* 1:2:2 sk-Alp14:αβ-tubulin:DRP reveals pseudo-dimeric head-to-tail subunits (red and orange) in a TOG square assembly consisting of four TOG domains bound to four αβ-tubulins (α-tubulin shown in cyan and β-tubulin shown in green) in a wheel-like organization. (A) Structure with DRP (yellow) bound to each αβ-tubulin. (B) Structure with DRP computationally removed. Each αβ-tubulin (α1β1) is positioned 90° rotated from its polymer-forming interface on its neighboring αβ-tubulin (α2β2). (C) Pseudo-dimeric TOG1-TOG2 subunits, shown in orange and red, respectively, form a head-to-tail TOG square (inset). Interface 1 is formed by the N-terminus of TOG2 and the TOG1-TOG2 linker binding to the C-terminus of the TOG1 domain of a second subunit, forming a 90° corner. Interface 2 is formed by the N-terminus of TOG1 binding the C-terminus of TOG2 within the same subunit in a 90° corner (Figure 2 Supplement 1I). (D) Rainbow view of TOG1-TOG2 with N- and C-termini displayed in a blue-to-red color gradient, while the other subunit is displayed in grey. Each TOG is composed of six HEAT repeats (numbered). (E) Close-up view of interface 1. A hydrophobic zone stabilizes interface1 (yellow and highlighted by red outline) involving Leu220 (L220) and Leu217 (L217) of the TOG1 inter-HEAT 5-6 loop, Leu179 (L179) of the HEAT 6 A-helix in TOG1 (red

ribbon) stabilized by linker residues (solid orange) Phe302 (F302), Leu304 (L304), and Leu305 (L305). An ionic zone guides interface 1 involving Glu219 (E219) of TOG1 inter-HEAT 5-6 loop and Glu305 (E305) of the TOG1-TOG2 linker, forming salt bridges with Lys346 (K346) and Lys347 (K347) of the TOG2 (light orange) inter-HEAT 1-2 loop and Arg390 (R390) of the TOG2 HEAT 2,3 loop, respectively. (F) Close-up view of interface 1, as in C, displaying residue conservation based on the alignment shown in Figure 2-Supplement 2. (G) Close-up view of interface 2. A hydrophobic zone stabilizes interface 1 involving Leu477 (L477) and Leu472 (L472) of the TOG2 inter-HEAT4-5 loop with Ile43 of the TOG1 inter-HEAT1-2 loop. Ionic zone selectively guides interface 2, involving Lys39 (K39) and Ser41 (S41) of the TOG1 inter-HEAT1-2 loop and helix 1B with Arg517 (R517), Glu518 (E518), Asp521 (D521), and Glu524 (E524) of the TOG2 inter-HEAT5-6 loop and A-helix. (H) Close-up view of interface 2, as in D, displaying reside conservation based on the alignment in Figure 2 Supplement 2.

Figure 3. Cysteine mutagenesis/crosslinking and mass spectrometry-based peptide-mapping reveal that dimeric sk-Alp14 forms TOG square conformations in solution.

(A) TOG square structure showing two cysteine pairs (green space fill) mutated in interfaces 1 (black-dashed lines) and 2 (red-dashed lines). (B) Close-up views of interfaces 1 (left) and 2 (right) showing the S180C-L304C and E518C-S41C residue pairs, respectively (green space fill), in sk-Alp14. (C) SDS-PAGE of SEC-purified sk-Alp14 S180C-L304C and E518C-S41C. (D) Crosslinking studies of

cysteine structural-based mutants using oxidizing conditions and αβ-tubulin binding, as denoted by (+) and (–). The αβ-tubulins form an intermediate in oxidizing conditions observed in all conditions that include αβ-tubulin (marked "*"). S180C-L304C sk-Alp14 forms a dimeric 170-kDa intermediate upon oxidization and αβ-tubulin binding (red arrow). In contrast, wt-Alp14 or sk-Alp14 E518C-S41C do not form this intermediate. (E) Disulfide peptide mapping of cysteines in sk-Alp14 S180C-L304C using differential alkylation and LC/MS-MS. We used mass spectrometry (LC/MS-MS) after a differential alkylation strategy (Figure 3 Supplement 1D) to map peptides with disulfides. Briefly, oxidized sk-Alp14 S180C-L304C (170-kDa) SDS-PAGE-purified bands were subjected to proteolysis and treated with iodoacetamide. Under these conditions, 57-Da in mass is added to peptides with reduced cysteines (free thiols), without affecting disulfides. Dithiothreitol was then used to reduce peptides with disulfides, which were then treated with 4-vinyl pyridine, which added 105-Da in mass to peptides with newly formed free thiols. Using LC/MS-MS, peptides with modified cysteines were identified based on added mass . Details provided in Figure 3 Supplement 1D.

Figure 4. Inactivation of interfaces 1 and 2 destabilizes TOG square organization without affecting αβ-tubulin binding. (A-D) Generation of structure-based TOG square assembly-defective mutants using wt-Alp14-dimer (A) through inactivation of interface 1 in the INT1 mutant (B: INT1, pink; 8 mutant residues), interface 2 in the INT2 mutant (C: INT2, green; 7 mutant residues), or

both interfaces 1 and 2 in the INT1+2 mutant (D: INT1+2, grey; 15 mutant residues). (E) Summary of SEC-measured αβ-tubulin binding molar ratios of INT1, INT2, and INT1+2 compared to wt-Alp14-dimer as described for Figure 1D suggests no defects in αβ-tubulin binding at 100 mM KCl (blue) and a similar decrease in αβ-tubulin binding upon 200 mM KCl ionic strength increase (cyan). Additional information is described in Figure 4 supplement 1. (F-H) Left, SEC-MALS INT1:αβ-tubulin (F), INT2:αβ-tubulin (G), and INT1+2: αβ-tubulin (H) complexes at 2:4 stoichiometry at 100 mM KCl (masses reported in Table 1): SEC-MALS reveals similar mass to wt-Alp14-dimer complexes with αβ-tubulin which are reported table 1. (I) Top, raw negative stain EM image of wt-Alp14-dimer:αβ-tubulin at 100 mM KCl reveals wheel-shaped assemblies that are 15-19 nm in diameter as previously described for Stu2-αβ-tubulin complexes (Al-Bassam et al., 2006). Second panel, 2D-classes reveal 19 nm wheel-shaped particles that match the 2D-projection of 30-Å resolution-filtered 2:4 TOG-square:αβ-tubulin complex (shown above the panel). These classes match the organization observed in the structure described in Figure 2. Bottom panel, second group of 2D-classes reveal small diamond-shaped particles that match the 2D-projection of a 30-Å resolution-filtered model of the TOG square without αβ-tubulins (shown above the panel). (J) raw images of INT1:αβ-tubulin reveal elongated conformations with either bent-conformations composed of bent-particles with two 8-nm densities at 90-degree angles or 16 nm filament-like particles. Second panel, 2D-classes reveal 16 nm elongated classes that match the 2D-projection of either 30-Å resolution-filtered TOG1-TOG2 bound to two

polymerized tubulins (shown above the second row) as described structurally in the next section. Left panel, 90-degree bend class averages that match 2D-projections of a resolution-filtered model of one TOG1-TOG2 subunit of the TOG square bound to two tubulins at 90 degrees (as shown above). Bottom panel, 2D-classes reveal 8-nm lengths, which match 2D-projections of low-resolution-filtered TOG-αβ-tubulin complexes (PDBID: 4FFB shown above the panel). (K) INT2 forms extended necklace shaped or extended 16 nm minifilaments. 2D-class averages reveal either 16-nm filament-like particles match 2D-projections of TOG1-TOG2 bound to two polymerized αβ-tubulins (left) or bent pbent particles that match 2D-projections of a bend TOG1-TOG2 subunit bound to two non-polymerized αβ-tubulins, as observed in half a TOG square complex (right). (L) INT1+2:αβ-tubulin complexes form only necklace-shaped assemblies with randomly interconnected 8-nm assemblies. Bottom panel, 2D-classes reveal 8 nm lengths, which match 2D-projections of low-resolution-filtered TOG-αβ-tubulin complexes (PDBID:4FFB shown above the panel). Additional information can be found in Figure 4 Supplement 1.

Figure 5. X-ray structure of 1:2:1 TOG-array:αβ-tubulin:DRPΔN reveals unfurled TOG1-TOG2 array bound to two polymerized αβ-tubulins. (A, B) Top, schemes of DRP and DRPΔN binding to αβ-tubulin. DRP shifts the equilibrium toward dissociation from αβ-tubulin. Bottom, isothermal titration calorimetery studies reveal a three-fold decrease in affinity of DRPΔN binding to αβ-tubulin (461 nM) compared to DRP (149 nM). (C, D) Two schematic views of

the TOG1-TOG2 αβ-tubulin complex transition from the TOG square (only half is shown) to the unfurled conformation upon DRPΔN dissociation. (E, F) Two orthogonal views of the 3.3-Å X-ray structure of 1:2:1 sk-Alp14 (red):αβ-tubulins (cyan and green):DRPΔN (yellow) complex, indicating a polymerized protofilament state. TOG2 and TOG1 are bound to the upper (α2β2) tubulin and lower (α1β1) tubulin, respectively.

Figure 6. Unfurling the TOG array: TOG2 rotation around TOG1 promotes the bound αβ-tubulins to polymerize. (A and B) Conformational change of TOG2 (blue) around TOG1 (red) while each is bound to αβ-tubulin (green and cyan) from a corner subunit in the wheel assembly (left) and in the extended conformation (right). TOG2 rotates 32° and translates 68 Å upon release to drive αβ-tubulin polymerization into a protofilament. (C) Superimposing unpolymerized αβ-tubulin (yellow) onto the α2β2-tubulin shows a conformational change in α-tubulin at the inter-dimer interface induced by polymerization. (D) Close-up view of the polymerized inter-dimer interface. Unpolymerized αβ-tubulin (yellow) is superimposed onto α2β2 (grey) of 1:2:1 structure. The α2-tubulin T7 loop and H8 helix engage the β1-tubulin GDP nucleotide through a T7 loop 5-Å translation and H8 helix 5° rotation involving residues Asp245 (D245), Gly246 (G246), Ala247 (A247), and Leu248 (L248).

Figure 7. Docking of atomic structures onto protofilament ends reveals the molecular details of unfurling. (A) Right, atomic model for four αβ-tubulin-

bound TOG square X-ray structures (Figure 2) docked using αβ-tubulin bound to TOG1 at the terminal αβ-tubulin in a curved protofilament (PDB ID: 3RYH). Left, magnified view of the zone of steric contact between TOG2-αβ-tubulin in the second subunit and the penultimate αβ-tubulin of the protofilament below the polymerization site. (B) Right, atomic model for four αβ-tubulin-bound TOG square X-ray structure (Figure 2) docked using αβ-tubulin bound to TOG2 at the terminal αβ-tubulin in a curved protofilament (PDB ID: 3RYH). Left, magnified view of the zone shown in A between TOG1-αβ-tubulin in the second subunit and the penultimate αβ-tubulin of the protofilament. Details and overlay images are shown in Figure 7 Supplement 1. (C) Docking the isolated TOG1-TOG2 two-αβ-tubulin assembly structure (extracted from the dimer structure) onto the terminal αβ-tubulin of the curved protofilament. (D) Docking of the unfurled 1:2:1 unfurled assembly structure (Figure 5) to the curved protofilament revealing TOG1 to be positioned at the base of the new assembly while TOG2 is positioned at the outer end of the newly formed MT plus-end.

Figure 8. A polarized unfurling model for TOG arrays as MT polymerases. An animation for this model is shown in Video S1. (A) Assembly of yeast MT polymerase dimeric TOG1-TOG2 subunits with four αβ-tubulins into an αβ-tubulin:TOG square. TOG squares diffuse along MT lattices modulated by tubulin C-termini interacting with SK-rich regions. (B) I. TOG square assemblies orient αβ-tubulins in wheel-shaped assemblies at MT plus-ends. II. These assemblies are destabilized upon TOG1-α-tubulin polymerizing onto the exposed β-tubulin at

MT plus-ends, releasing TOG1-TOG2 subunits in corner conformations. III. The release of TOG2:αβ-tubulin allows free rotation around TOG1, driving two αβ-tubulins to polymerize. IV. TOG2 dissociates from the newly polymerized αβ-tubulin stabilizing protofilament at the plus-end while TOG1 anchors this αβ-tubulin onto the MT plus-end. V. Straightening of this new protofilament leads to the dissociation of TOG1. The rebinding of TOG1-TOG2 subunits to αβ-tubulins reforms the TOG square assembly and restarts the MT polymerase cycle. Atomic views for states I, II, and III are shown in Figure 7.

Supplementary Tables:

Table S1: Masses of the αβ-tubulin-bound Alp14 TOG array constructs

Table S2: Binding capacities of Alp14 constructs for αβ-tubulins

Table S3: X-ray crystallographic and refinement statistics for structures

Table S4: Buried surface area between αβ-tubulin and TOG domains or DRP

Table S5: Intra- and inter-dimer curvature angles of αβ-tubulins in structures

Video Description

Video 1: Animation of the mechanism of polarized unfurling for multiple TOG domains in a yeast MT polymerase. This animation describes the "polarized unfurling" mechanism for multiple TOG domains in promoting MT polymerization. Briefly, Yeast MT polymerases are dimers with each subunit including TOG1 and TOG2 domains separated by a linker and followed by unstructured SK-rich and coiled-coil domains. Each MT polymerase binds four αβ-tubulins forming TOG square assemblies, as shown in the ribbon diagram (Figure 2). TOG2 exchanges αβ-tubulin due to its rapid exchange rate, while TOG square assemblies diffuse along MT lattices loaded with αβ-tubulins at MT plus-ends, as visualized in Figure 8. Docking of TOG square assemblies via TOG2 αβ-tubulin does not destabilize the TOG square as described in Figure 7. The polymerization of αβ-tubulin-TOG1 destabilizes TOG square complexes at interface 1 due to steric contact as described in Figure 7. The destabilization of the TOG square releases TOG2, promoting polarized unfurling of two soluble αβ-tubulins into one curved protofilament at the MT plus-end, as visualized in Figure 5. The newly formed protofilament is further stabilized by the rapid dissociation of TOG2 from the outermost αβ-tubulin, and forms corners to enhance direct αβ-tubulin polymerization at the MT plus-end. Other MT polymerase molecules promote delivery of αβ-tubulin dimers via the “polarized unfurling” mechanism at polymerizing MT plus-ends. Individual steps for this model are shown in Figure 8.

Legends for figure supplements

Figure 1 Supplement 1 (Fig1-S1): The Alp14 TOG array:αβ-tubulin binding capacities reveal non-equivalent behavior of TOG1 and TOG2 in different conditions.

We determined the molar ratio for four Alp14 constructs (described in Figure 1) in binding to soluble αβ-tubulins at 100 and 200 mM KCl conditions using quantitative-size exclusion chromatography (SEC). Values for molar ratios are reported in Figure 1D and Table S2 revealing the molar ratios of αβ-tubulin bound to these Alp14 constructs. In each condition, 1 μmol of each Alp14 construct was mixed with a defined αβ-tubulin amount (1 μmol per Alp14 subunit) in each condition, and then analyzed by SEC as shown in A, D, G, and J. The SDS-PAGE results for fractions are shown in B, E, H, and K.

(**A, D, G, J)** Top, models for Alp14 constructs studied for tubulin binding using SEC: (A) Alp4-monomer (residues 1-510), (B) wt-Alp14-dimer (residues 1-690), (C) TOG1M (TOG1-inactivated Alp14-dimer mutant), and (D) TOG2M (TOG2-inactivated Alp14-dimer mutant). Bottom, SEC-elution profiles for these constructs in complex with αβ-tubulin at 80-100 and 200 mM KCl at the ratios of TOG array subunit:αβ-tubulin described for each condition. Note that the largest Alp14:αβ-tubulin complexes are observed at 100 mM KCl in 1:2 molar ratio for Alp14-monomer, and 2:4 molar ratio for wt-Alp14-dimer constructs. Molar ratios are shown and colored according to each SEC trace.

(B, E, H, K) Compositions of SEC fractions shown in each panel above (A, D, G, and J) using SDS-PAGE. Molar ratios for Alp14:αβ-tubulin are shown in the

same colors as the traces above. The SDS-PAGE analyses reveal that αβ-tubulin dissociates at 200 mM KCl, forming a second peak due to dissociation at 200 mM KCl. Note that TOG1M fully dissociates from αβ-tubulin at 200 mM, while TOG2M remains mostly bound to αβ-tubulin at 200 mM KCl. Molar ratios of Alp14 to αβ-tubulin were determined using quantitative densitometry at those conditions and reported in Table S2 and Figure 1D.

(**C, H, I, L)** Schematic models, similar to Figure 1F, for Alp14-monomer, wt-Alp14-dimer, TOG1M, and TOG2M in binding αβ-tubulins at 100 mM and 200 mM KCl, revealing the non-equivalent behavior of TOG1 and TOG2 domains in binding and releasing αβ-tubulins in response to different ionic strengths.

Figure 1 Supplement 2 (Fig1-S2): **Molar ratios of Alp14 constructs binding to αβ-tubulin binding in the presence of Darpin-D1 (DRP) show no change in stoichiometry, and control SEC-MALS traces.**

For each condition, 1 μmol of each Alp14 construct (described in Figure 1) was mixed with defined molar amount of soluble αβ-tubulin (1-2 μmol moles per Alp14 subunit) and Darpin-D1 (DRP).

(A, D) Top shows models for DRP (yellow) binding to Alp14 constructs: (A) Alp14-monomer (1-510) and (B) wt-Alp14-dimer (residues 1-690). Bottom, SEC elution profiles for Alp14 constructs in complex with αβ-tubulin at 80-100 and 200 mM KCl at two molar ratios described for each condition. Molar ratios are shown and colored according to each SEC trace. Colors for each of the traces match the ratios reported at the top left of each SDS-PAGE panel described below.

Note that αβ-tubulin dissociates into a second peak in the 200 mM KCl condition, similar to conditions without DRP described in Figure 1 Supplement 1 (Fig1-S1).

(B, E) SDS-PAGE of the four SEC traces shown in A and D, respectively: Alp14 monomer:αβ-tubulin (B) and Alp14-dimer:αβ-tubulin complexes (E). Top left corner shows the molar ratio in the same color as the trace above. Note that DRP binds αβ-tubulins in each Alp14:αβ-tubulin complex, and that its stoichiometry matches αβ-tubulin. Note the dissociation of αβ-tubulin-DRP from Alp14 constructs, which forms a second peak at 200 mM KCl.

(C, F) Schematic models for Alp14-monomer and Alp14-dimer in binding αβ-tubulins at 80-100 mM and 200 mM KCl, revealing the non-equivalent behavior of TOG1 and TOG2 domains in releasing αβ-tubulins. DRP can access each β-tubulin interface, suggesting that TOG arrays maintain αβ-tubulins in a non-polymerized state upon binding.

To find the effect of DRP binding to Alp14: β-tubulin complex, we determined the molar ratios for two Alp14 constructs binding to αβ-tubulins at 100 and 200 mM KCl conditions in the presence of DRP by quantitative-SEC using panels B and F. The values for molar ratios are reported in Figure 1D and Table S2, revealing molar ratios of αβ-tubulin bound to two Alp14 constructs were not influenced by DRP binding to αβ-tubulin. This finding suggests that αβ-tubulin binds to TOG arrays in a dimeric and non-polymerized state initially.

(G) SEC-MALS traces for isolated Alp14-monomer, αβ-tubulin, and wt-Alp14-dimer revealing their masses at 200 mM KCl. These data are summarized in Table S1. Alp14-monomer is indeed monomeric, while wt-Alp14-dimer is

homodimeric and αβ-tubulin is a heterodimer. SEC-MALS measured masses are reported in Table S1.

(H) SEC-MALS traces for Alp14-dimer binding to αβ-tubulin at a 2:2 molar ratio with 100 mM KCl or 200 mM KCl, respectively. These data are summarized in Table S1.

Figure 1 Supplement 3 (Fig1-S3): **Isothermal titration calorimetry (ITC) reveals Alp14-TOG1 and TOG2 αβ-tubulin binding affinities.**

(A) Top and bottom panels: scheme for recombinant TOG1 and TOG2 domains studied and SDS-PAGE of purified 10 and 1 μM TOG1 and TOG2 domains, respectively.

(B) Summary of measured αβ-tubulin binding affinities at 100 and 200 mM KCl.

(C, E) ITC traces for TOG1 (blue) binding to αβ-tubulin showing enthalpy and entropy measured at 100 and 200 mM KCl.

(D, F) Isothermal titration calorimetry traces for TOG2 (cyan) binding to αβ-tubulin showing enthalpy and entropy measured at 100 and 200 mM KCl.

Figure 2 Supplement 1 (Fig2-S1): X-ray crystallography and structure determination of 2:4:4 Alp14-monomer:αβ-tubulin:DRP complexes.

(A) Images of square crystals of 1:2:2 sk-Alp14-monomer:αβ-tubulin:DRP assemblies.

(B) Molecular replacement search results for αβ-tubulin placement in the asymmetric unit. Note the distinct solution that leads to initial positioning.

(C) Molecular replacement search results for the TOG domain in the asymmetric unit.

(D) Initial density map of electron density for the TOG square assembly after the placement of TOG domains based on initial molecular replacement. Note the presence of only the essential features of both TOG domains.

(E) Density map of the TOG square assembly after one cycle of density modification. Note the appearance of density of the linker and associating interfaces. Density maps reveal TOG1 based on its C-terminal extension and jutting C-terminal α-helix.

(F) Top view along *b* axis of the crystallographic unit cell revealing the packing arrangement of two 2:4:4 sk-Alp14-monomer:$\alpha\beta$-tubulin:DRP wheel-shaped complexes in the asymmetric unit, shown in multiple colors. Bottom, a 90° rotation of the view in **F**, revealing the unit cell packing showing 2D sheets of wheel-shaped complexes.

(G) 4.4-Å resolution 2Fo-Fc electron density contoured at 1 σ of the native 2:4:4 sk-Alp14-monomer:$\alpha\beta$-tubulin:DRP structure.

(H) 3.6-Å resolution 2Fo-Fc electron density contoured at 1 σ of the 2:4:4 sk-Alp14-SL:$\alpha\beta$-tubulin:DRP structure. Both **G** and **H** show the organization of the assembly and the modeled subunits.

(I) Detailed close-up views of the electron density map in **H**. Top, view of TOG1 (orange)-TOG2 (red) in interface 1. The linker sequence is depicted as red with green density (difference Fourier map). Bottom, detailed view of DRP (yellow) in

proximity to the α-tubulin of a neighboring TOG-bound αβ-tubulin (blue). Note the lack of interactions between DRP and α-tubulin.

(J) View of DRP proximity to the α-tubulin of the neighboring tubulin dimer. Note that the distances of residues are beyond 3.5 Å in most cases, showing no pattern of direct interactions.

(K) View of second DRP of a non-crystallographic symmetry mate in the same orientation as shown in I.

Figure 2 Supplement 2 (Fig2-S2): Sequence conservation in TOG square interfaces across each TOG1 and TOG2 domain.

(A) Top scheme for Alp14, TOG1, TOG2, and linker sequence. Bottom, structure of TOG square with two TOG1 (blue) and two TOG2 (cyan) domains forming interfaces via inter-HEAT repeat elements with the TOG1-TOG2 linker sequence (red).

(B) Sequence alignment of TOG1-TOG2 across multiple species with the invariant residues shown in purple, highly conserved residues in blue, weakly conserved residues in cyan, and non-conserved residues in black. The secondary structures (Cylinders, α-helices; lines, random coil; and dashed lines, disordered segments) are described above the sequences. Interfaces 1 and 2 are highlighted in black and red boxes, respectively. Xl, *Xenopus laveis (marked green)*; Hs, *Homo sapiens*; Dm, *Drosophila melanogaster*; Sp, *S. pombe (marked red)*; Ct, *Chaetomium thermophilum*; An, *Aspergillus nidulans*; Kl, *Kluyveromyces lactis*; Ag, *Ashbya gossypii*; Kw, *Kluyveromyces waltii*; Sk, *Saccharomyces kluyveri* (marked blue), Scas, *Shorea crassa*; Sc, *S. cerevisiae*.

Figure 3 Supplement 1 (Fig3-S1): Yeast dimeric TOG arrays form a TOG square assembly in solution as measured by cysteine crosslinking and mass spectrometry.

(A) Mass spectrometry-based strategy for disulfide peptide mapping for the sk-Alp14 S180C L304C mutant reveals that sequences of peptides in interface 1 form crosslinked disulfides, confirming that the conformation of interface 1 is observed in solution. Top, chemical modification strategy for differential alkylation to modify cysteines and detect disulfides.

(B) LC/MS-MS traces for two peptides showing the mass units identifying these peptides with cysteines modified by alkylation with a mass of 105-Da.

Figure 4 Supplement 1 (Fig4-S1): Inactivating interfaces 1 and 2 destabilizes the TOG square organization but does not influence αβ-tubulin binding activity.

(A) Purification of INT1 mutant. Top, SEC-elution profile and trace for INT1 showing that it behaves homogenously similarly to wt-Alp14-dimer. Bottom panel show SDS-PAGE for SEC purified fractions.

(B) Purification of INT2 mutant. Top, SEC-elution profile and trace for INT2 showing that it behaves homogenously similarly to wt-Alp14-dimer. Bottom panel shows SDS-PAGE of SEC purified fractions.

(C) Purification of INT12 mutant. Top, SEC-elution profile and trace for INT12 showing that it behaves homogenously similarly to wt-Alp14-dimer. Bottom panel shows SDS-PAGE of SEC purified fractions.

(D) SEC traces for INT1:αβ-tubulin complexes at 100 (light pink) and 200 mM KCl (dark pink) at 2:4 molar ratio showing that inactivating the TOG square assembly has little effect on αβ-tubulin binding. Note that roughly half the αβ-tubulin dissociates at 200 mM KCl due to rapid exchange by TOG2. SDS-PAGE for fractions are shown below.

(E) SEC traces for INT2:αβ-tubulin complexes at 100 (light green) and 200 mM KCl (dark green) at 2:4 molar ratio showing that inactivating the TOG square assembly has little effect on αβ-tubulin binding. Note that roughly half the αβ-tubulin dissociates at 200 mM KCl due to rapid exchange by TOG2. SDS-PAGE for fractions are shown below.

(F) SEC traces for INT12:αβ-tubulin complexes at 100 (light grey) and 200 mM KCl (dark grey) at 2:4 molar ratio showing that inactivating the TOG square assembly has little effect on αβ-tubulin binding. Note that roughly half the αβ-tubulin dissociates at 200 mM KCl due to rapid exchange by TOG2. SDS-PAGE for fractions are shown below.

Figure 4 Supplement 2 (Fig4-S2): Negative stain EM micrographs and class averages for the TOG square and its inactivated assemblies.

(A), (D), (G), and (J) Raw negative stain EM micrographs of WT-Alp14-dimer:αβ-tubulin, INT1, INT2, and INT12, respectively. Note that the highlighted rectangle

regions are shown in Figure 1. Boxes (yellow and red) indicate representative examples of wheel-shaped, TOG-square, unfurled TOG-array, and single TOG:αβ-tubulin assemblies, respectively.

(B) and (C) Class averages of negatively stained WT-Alp14-dimer:αβ-tubulin complex as calculated by CryoSparc, confirming that wheel-shaped (red circle) and TOG square (yellow circle) assemblies exist in solution.

(E) and (F) Class averages of negatively stained INT1:αβ-tubulin complex as calculated by CryoSparc, revealing multiple conformations of INT1:αβ-tubulin complex (Unfurled TOG array or half-TOG square, red circle; single TOG:αβ-tubulin, yellow circle).

(H) and (I) Class averages of negatively stained INT2:αβ-tubulin complex as calculated by CryoSparc, revealing multiple conformations of INT2:αβ-tubulin complex (Unfurled TOG array or half-TOG square, red circle; single TOG:αβ-tubulin, yellow circle).

(K) Class averages of negatively stained INT12:αβ-tubulin complex as calculated by CryoSparc. This finding shows only single TOG:αβ-tubulin conformations (yellow circle), suggesting that interfaces 1 and 2 are required for higher order assemblies.

Bars shown at the lower right hand corner for panels A, D, G, and J are 25 nm; while bars for panels B, C, E, F, H, I, and K are 10 nm.

Figure 5 Supplement 1 (Fig5-S1): Strategy to promote αβ-tubulin polymerization using DRPΔN and the structural comparison of DRP and DRPΔN interfaces with αβ-tubulin.

(A) SEC trace for the purified DRPΔN mutant.

(B) SEC trace of 1:2:2 TOG1-TOG2:αβ-tubulin:DRPΔN complex (blue) in comparison to DRPΔN (red) and αβ-tubulin (black).

(C) and (**D)** SDS-PAGE fractions shown in A and B, respectively.

(E) Models of the DRPΔN (orange) and DRP (yellow). Comparison of their binding interfaces with αβ-tubulin dimer reveals 20% decrease interface size.

(F) View of αβ-tubulin binding interfaces of DRPΔN (orange) and DRP (yellow). Note the decrease in interface surface at the fifth ankyrin repeat.

Figure 5 Supplement 2 (Fig5-S2): X-ray crystallographic structure determination of 1:2:1 Sk-Alp14-monomer:αβ-tubulin:DRPΔN complex .

(A) View of rectangular 1:2:1 TOG1-TOG2:αβ-tubulin:DRPΔN crystals formed in the same conditions as crystals in Figure Fig2-S1.

(B) Top, molecular replacement solution to identify positions for αβ-tubulin in the in the asymmetric unit. Bottom, molecular replacement solution to identify positions for TOG domains in the asymmetric unit.

(C) 3.3-Å resolution refined 2Fo-Fc density map with 1 σ contour of the native 1:2:1 TOG1-TOG2:αβ-tubulin:DRPΔN assembly showing the organization of the extended assembly and the modeled protein subunits.

(D) Top, top-end view of the unit cell packing arrangement of 1:2:1 TOG1-TOG2: αβ-tubulin:DRPΔN extended complexes (shown in multiple colors). Bottom, 90° rotation with extended packing leads to side view of the unit cell arrangement. **(E)** The TOG1-TOG2 polymerized αβ-tubulin (red) structure is highly curved compared to most known αβ-tubulin polymers, such as assemblies of stathmin/RB3 complexes (GDP in cyan and GTP in yellow) and straight MT protofilaments (green). An analysis similar to that previously published (Brouhard and Rice, 2014) was used to compare the protofilament curvatures. Data are also described in Table S5.

Figure 7 Supplement 1 (Fig7-S1): All-atom docking models for structures superimposed onto curved protofilament plus-ends.

(A) An all-atom model for a TOG square bound to four αβ-tubulins docked onto the protofilament plus-end by overlaying the terminal αβ-tubulin with the αβ-tubulin bound onto TOG1. Note some minor steric clashes between TOG2-αβ-tubulin from the second αβ-tubulin and penultimate αβ-tubulin in the protofilament (green arrows). These steric contacts may induce destabilization of the TOG square at interface 1 near the site of polymerization.

(B) An all-atom model for a TOG square bound to four αβ-tubulins docked onto the protofilament plus-end by overlaying the terminal αβ-tubulin with the αβ-tubulin bound onto TOG2. Note the TOG1-αβ-tubulin from the second αβ-tubulin is retracted 10-Å away from the penultimate αβ-tubulin in the protofilament

(green arrows). This finding suggests that TOG2-αβ-tubulin docking has no effect on destabilizing the TOG square.

(C) An overlay of A and B is shown.

Supplementary Reference:

Brouhard, G.J., and Rice, L.M. (2014). The contribution of alphabeta-tubulin curvature to microtubule dynamics. J Cell Biol *207*, 323-334.

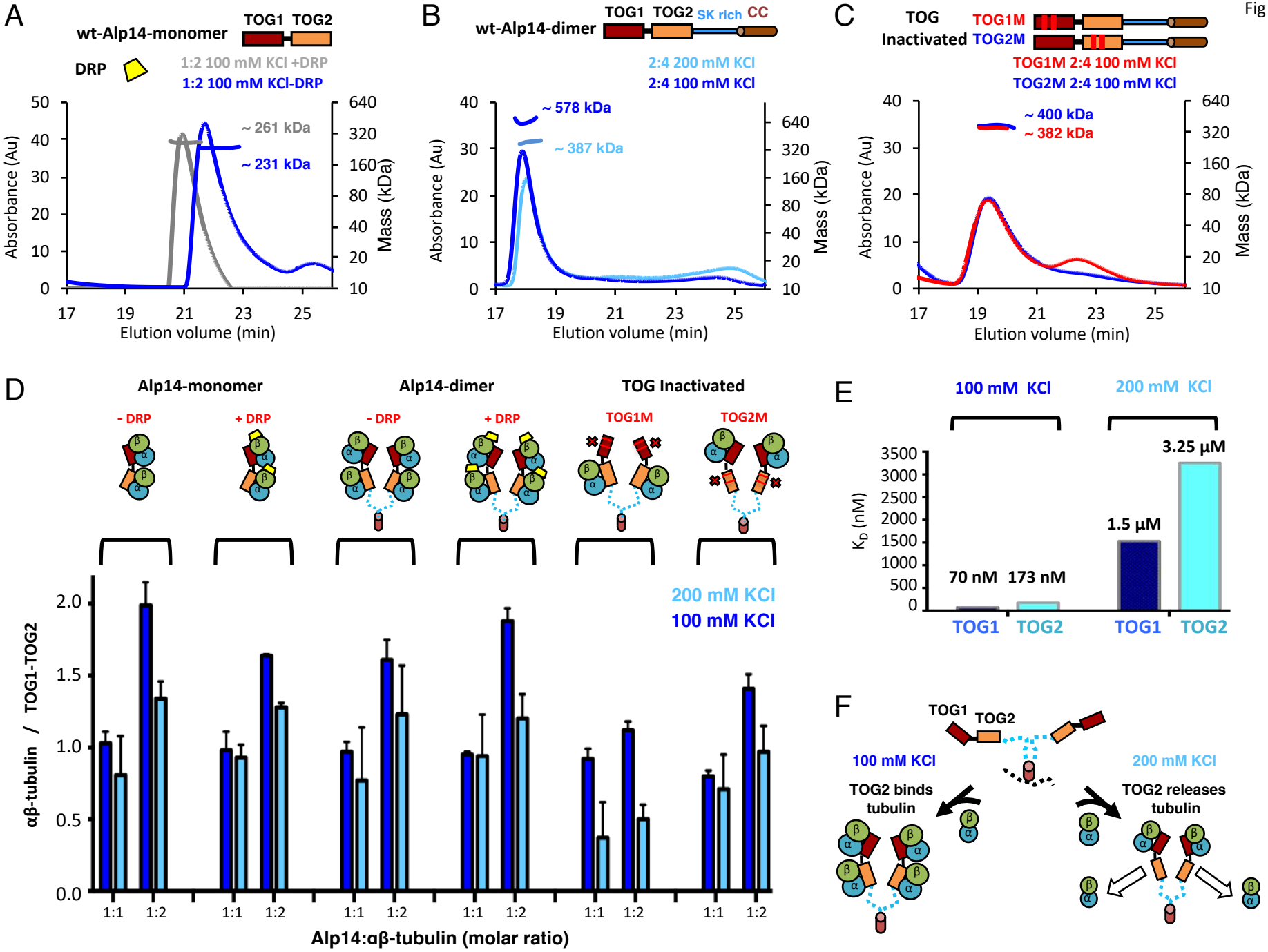
A
wt-Alp14-monomer
TOG1 TOG2
DRP
1:2 100 mM KCl +DRP
1:2 100 mM KCl-DRP
~ 261 kDa
~ 231 kDa
Absorbance (Au)
Mass (kDa)
Elution volume (min)
B
wt-Alp14-dimer
TOG1 TOG2 SK rich CC
2:4 200 mM KCl
2:4 100 mM KCl
~ 578 kDa
~ 387 kDa
C
TOG Inactivated
TOG1M
TOG2M
TOG1M 2:4 100 mM KCl
TOG2M 2:4 100 mM KCl
~ 400 kDa
~ 382 kDa
D
Alp14-monomer
Alp14-dimer
TOG Inactivated
- DRP
+ DRP
TOG1M
TOG2M
200 mM KCl
100 mM KCl
αβ-tubulin / TOG1-TOG2
Alp14:αβ-tubulin (molar ratio)
E
100 mM KCl
200 mM KCl
K_D (nM)
70 nM
173 nM
1.5 µM
3.25 µM
TOG1
TOG2
F
TOG1
TOG2
100 mM KCl
200 mM KCl
TOG2 binds tubulin
TOG2 releases tubulin

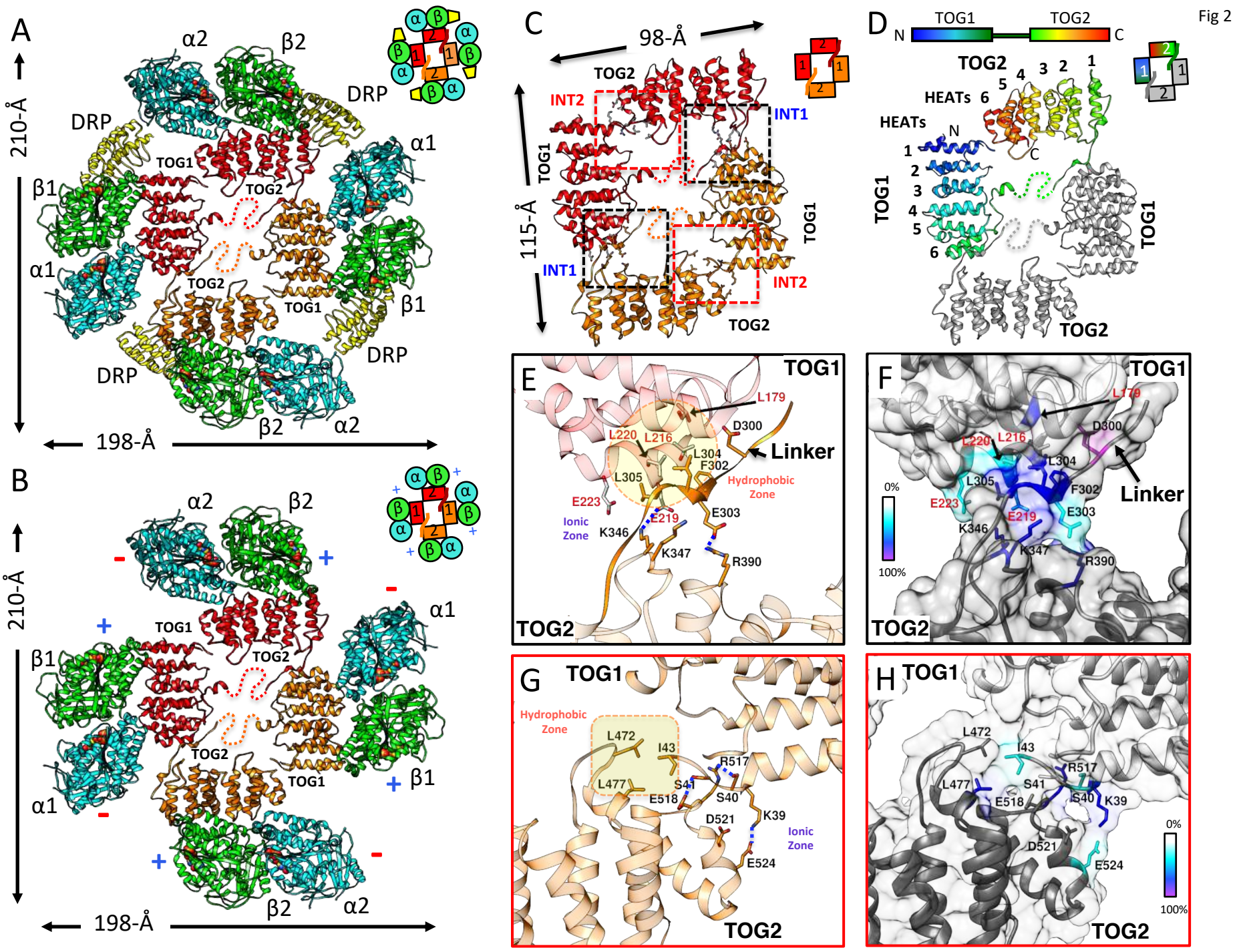
A
α2
β2
DRP
DRP
α1
TOG1
TOG2
β1
α1
TOG2
TOG1
β1
DRP
DRP
β2
α2
210-Å
198-Å
B
α2
β2
α1
TOG1
TOG2
β1
α1
TOG2
TOG1
β1
β2
α2
210-Å
198-Å
C
98-Å
TOG2
INT2
INT1
TOG1
TOG1
115-Å
INT1
INT2
TOG2
D
N
TOG1
TOG2
C
TOG2
HEATs
HEATs
N
C
TOG1
TOG1
TOG2
E
TOG1
L179
D300
L220
L216
L304
F302
Linker
L305
Hydrophobic
Zone
E223
Ionic
Zone
K346
E219
E303
K347
R390
TOG2
F
TOG1
L179
D300
L220
L216
L304
0%
L305
F302
Linker
E223
E219
E303
K346
K347
R390
100%
TOG2
G
TOG1
Hydrophobic
Zone
L472
I43
R517
L477
S41
E518
S40
D521
K39
Ionic
Zone
E524
TOG2
H
TOG1
L472
I43
R517
L477
S41
E518
S40
K39
0%
D521
E524
100%
TOG2

Fig 2

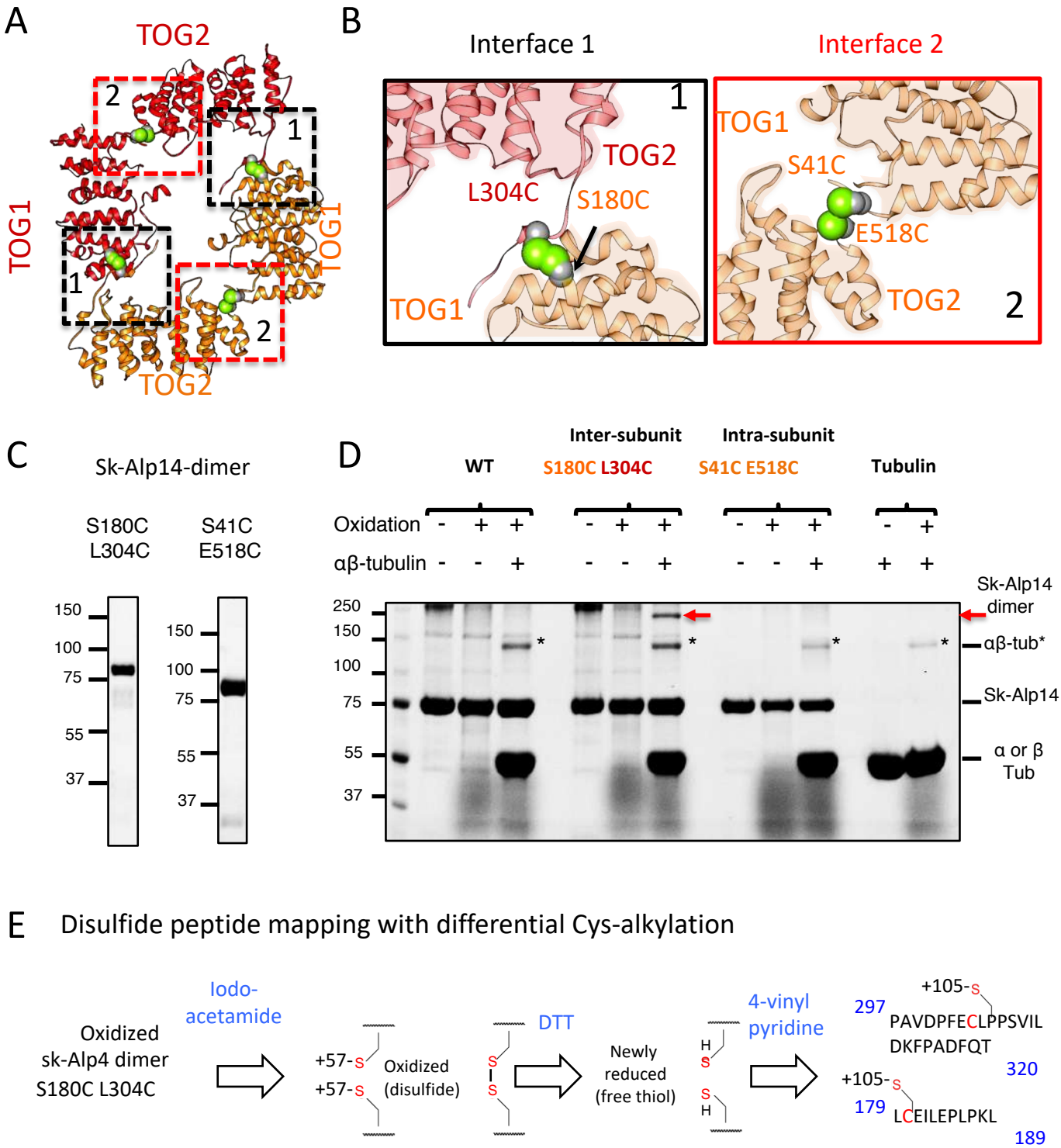
A
TOG2
TOG1
TOG1
TOG2
1
2
1
2
B
Interface 1
Interface 2
1
TOG2
L304C
S180C
TOG1
TOG1
S41C
E518C
TOG2
2
C
Sk-Alp14-dimer
S180C
L304C
S41C
E518C
150
100
75
55
37
150
100
75
55
37
D
Inter-subunit
Intra-subunit
WT
S180C L304C
S41C E518C
Tubulin
Oxidation - + + - + + - + + - +
αβ-tubulin - - + - - + - - + + +
250
150
100
75
55
37
Sk-Alp14 dimer
αβ-tub*
Sk-Alp14
α or β Tub
E
Disulfide peptide mapping with differential Cys-alkylation
Oxidized
sk-Alp4 dimer
S180C L304C
Iodo-
acetamide
+57-S
+57-S
Oxidized
(disulfide)
DTT
Newly
reduced
(free thiol)
4-vinyl
pyridine
+105-S
297
PAVDPFECLPPSVIL
DKFPADFQT
320
+105-S
179
LCEILEPLPKL
189

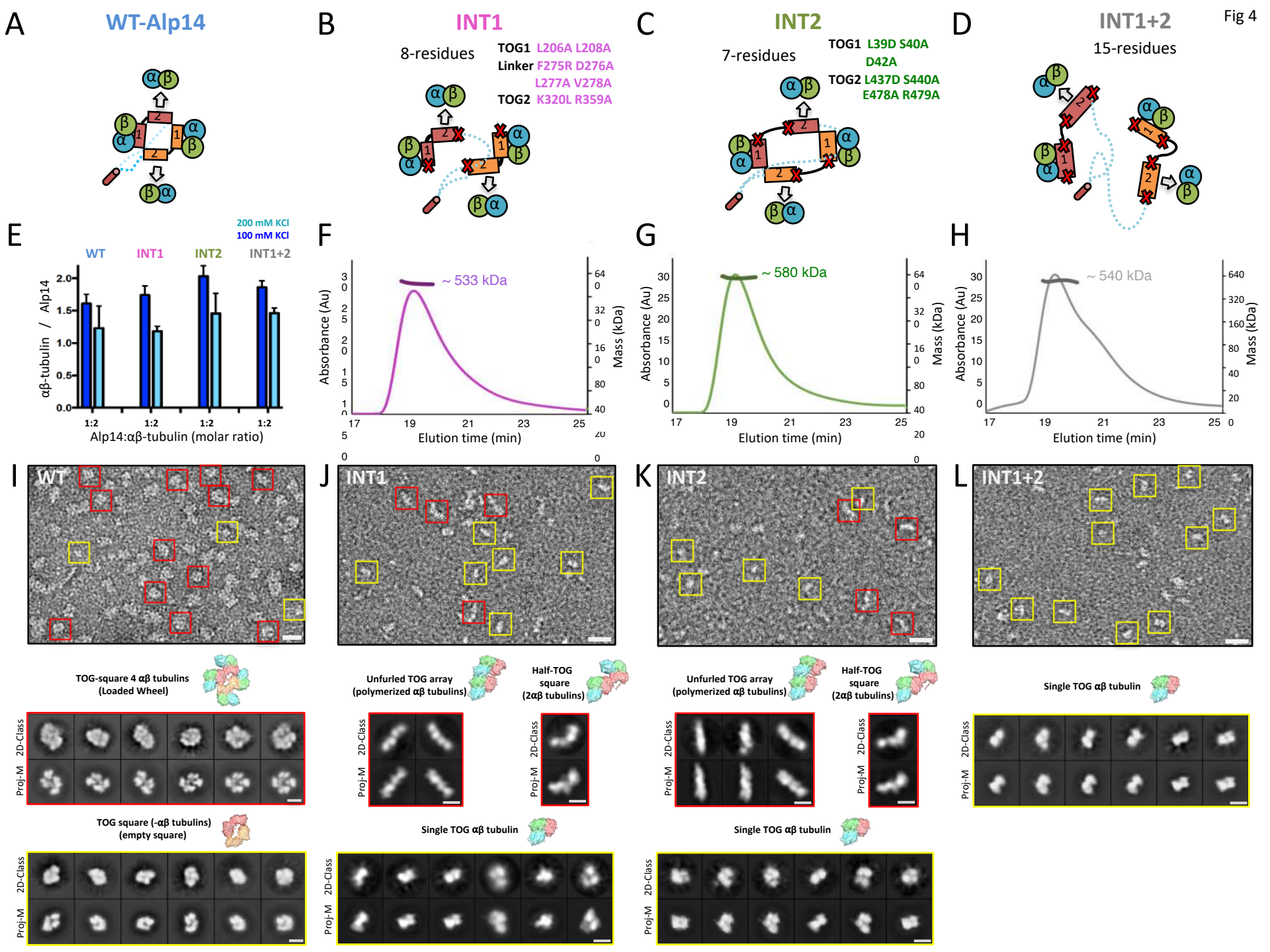
A
WT-Alp14
B
INT1
8-residues
TOG1 L206A L208A
Linker F275R D276A
L277A V278A
TOG2 K320L R359A
C
INT2
7-residues
TOG1 L39D S40A
D42A
TOG2 L437D S440A
E478A R479A
D
INT1+2
15-residues
E
200 mM KCl
100 mM KCl
WT
INT1
INT2
INT1+2
αβ-tubulin / Alp14
Alp14:αβ-tubulin (molar ratio)
F
~ 533 kDa
G
~ 580 kDa
H
~ 540 kDa
Absorbance (Au)
Mass (kDa)
Elution time (min)
I
WT
J
INT1
K
INT2
L
INT1+2
TOG-square 4 αβ tubulins
(Loaded Wheel)
Unfurled TOG array
(polymerized αβ tubulins)
Half-TOG
square
(2αβ tubulins)
Single TOG αβ tubulin
TOG square (-αβ tubulins)
(empty square)
2D-Class
Proj-M

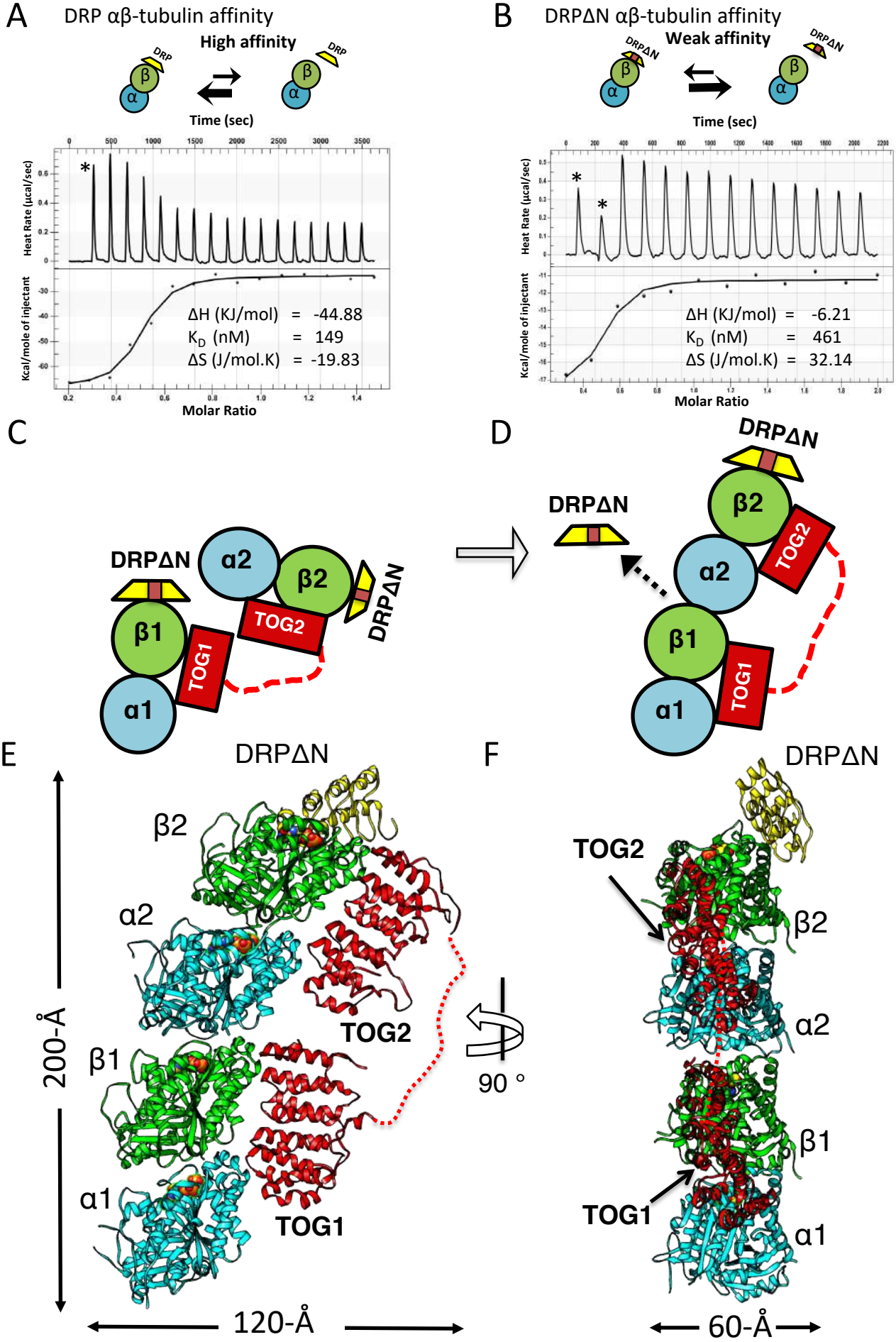
A
DRP αβ-tubulin affinity
High affinity
DRP
DRP
Time (sec)
Heat Rate (µcal/sec)
Kcal/mole of injectant
ΔH (KJ/mol) = -44.88
K_D (nM) = 149
ΔS (J/mol.K) = -19.83
Molar Ratio
B
DRPΔN αβ-tubulin affinity
Weak affinity
DRPΔN
DRPΔN
Time (sec)
Heat Rate (µcal/sec)
Kcal/mole of injectant
ΔH (KJ/mol) = -6.21
K_D (nM) = 461
ΔS (J/mol.K) = 32.14
Molar Ratio
C
DRPΔN
α2
β2
β1
TOG2
TOG1
α1
DRPΔN
D
DRPΔN
DRPΔN
β2
TOG2
α2
β1
TOG1
α1
E
DRPΔN
β2
α2
TOG2
β1
α1
TOG1
200-Å
120-Å
90 °
F
DRPΔN
TOG2
β2
α2
β1
TOG1
α1
60-Å

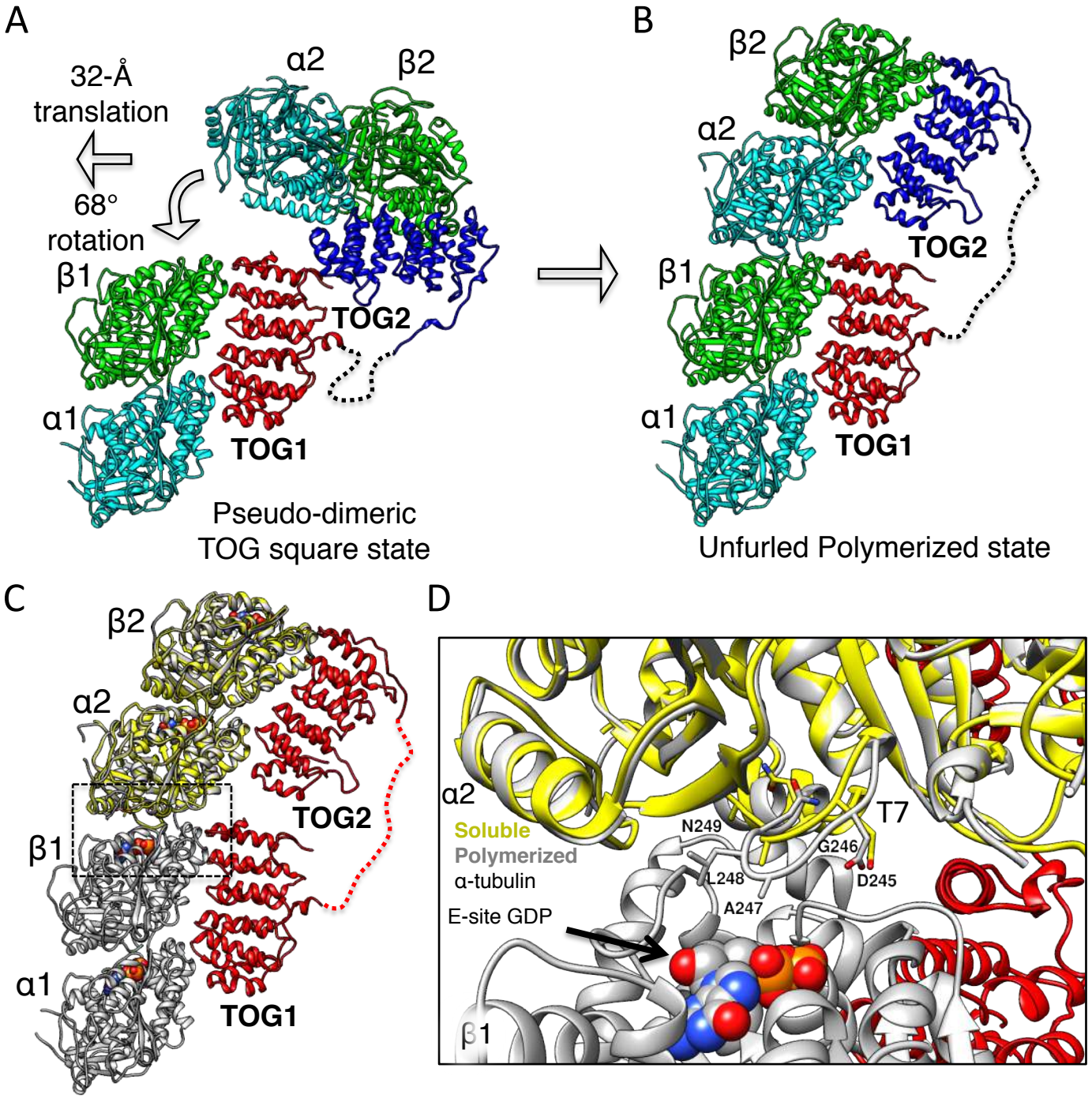
A
32-Å
translation
68°
rotation
α2
β2
β1
TOG2
α1
TOG1
Pseudo-dimeric
TOG square state
B
β2
α2
TOG2
β1
α1
TOG1
Unfurled Polymerized state
C
β2
α2
TOG2
β1
α1
TOG1
D
α2
Soluble
Polymerized
α-tubulin
E-site GDP
N249
T7
G246
L248
D245
A247
β1

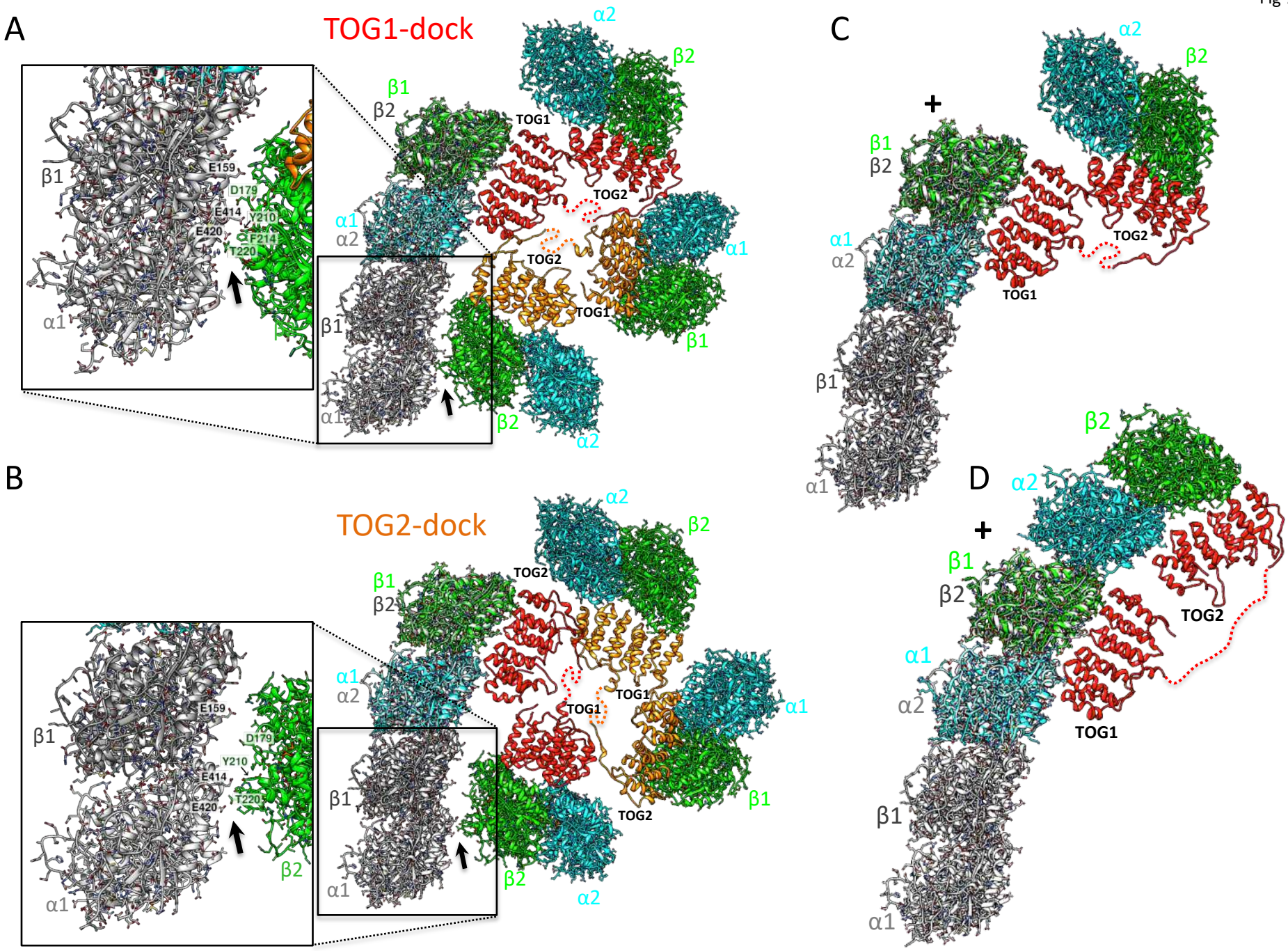
A
TOG1-dock
B
TOG2-dock
C
D
α1
α2
β1
β2
TOG1
TOG2
E159
D179
E414
Y210
E420
F214
T220

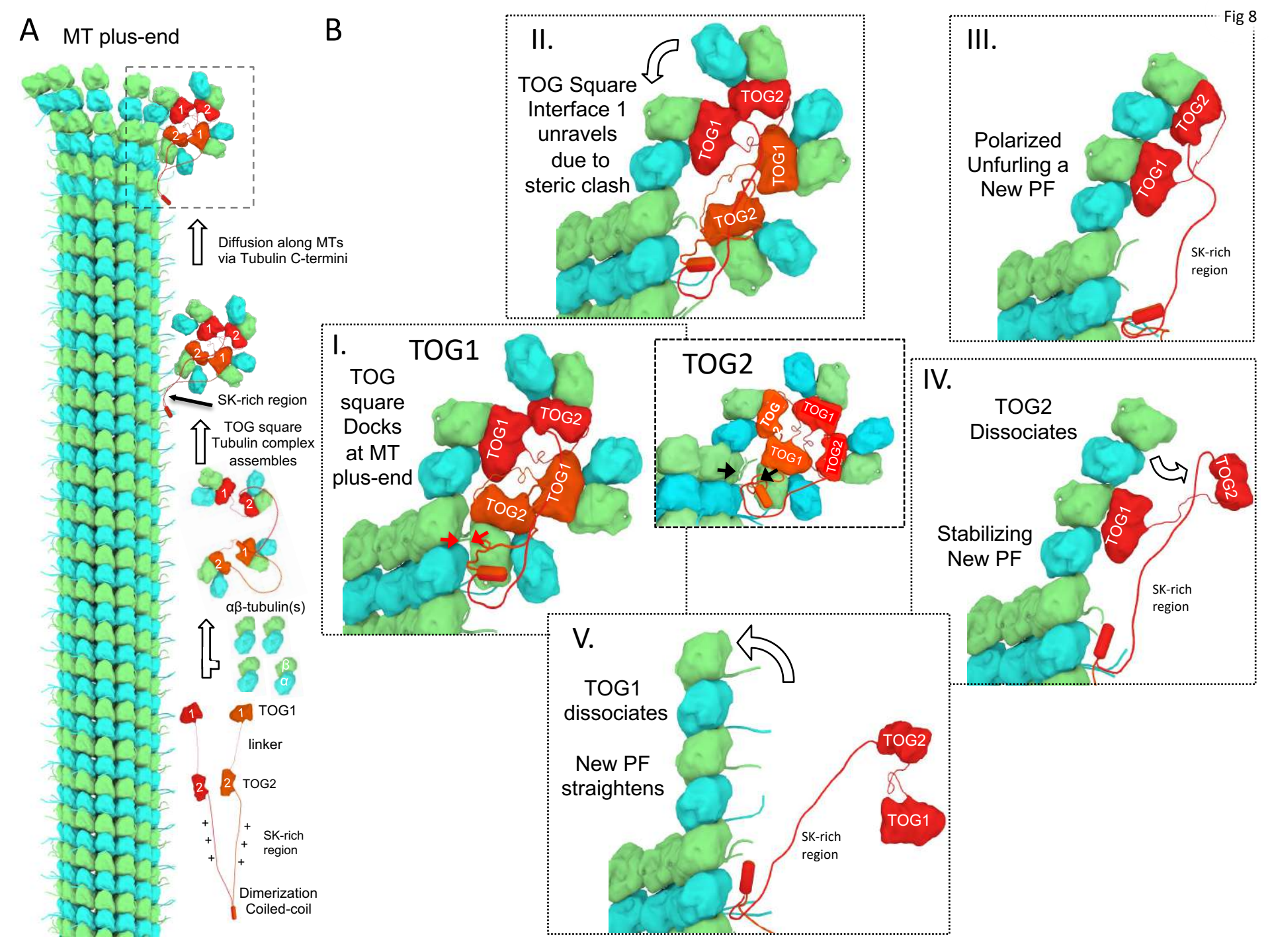
A
MT plus-end
Diffusion along MTs
via Tubulin C-termini
SK-rich region
TOG square
Tubulin complex
assembles
αβ-tubulin(s)
TOG1
linker
TOG2
SK-rich
region
Dimerization
Coiled-coil
B
I.
TOG1
TOG
square
Docks
at MT
plus-end
TOG2
II.
TOG Square
Interface 1
unravels
due to
steric clash
III.
Polarized
Unfurling a
New PF
SK-rich
region
IV.
TOG2
Dissociates
Stabilizing
New PF
SK-rich
region
V.
TOG1
dissociates
New PF
straightens
SK-rich
region

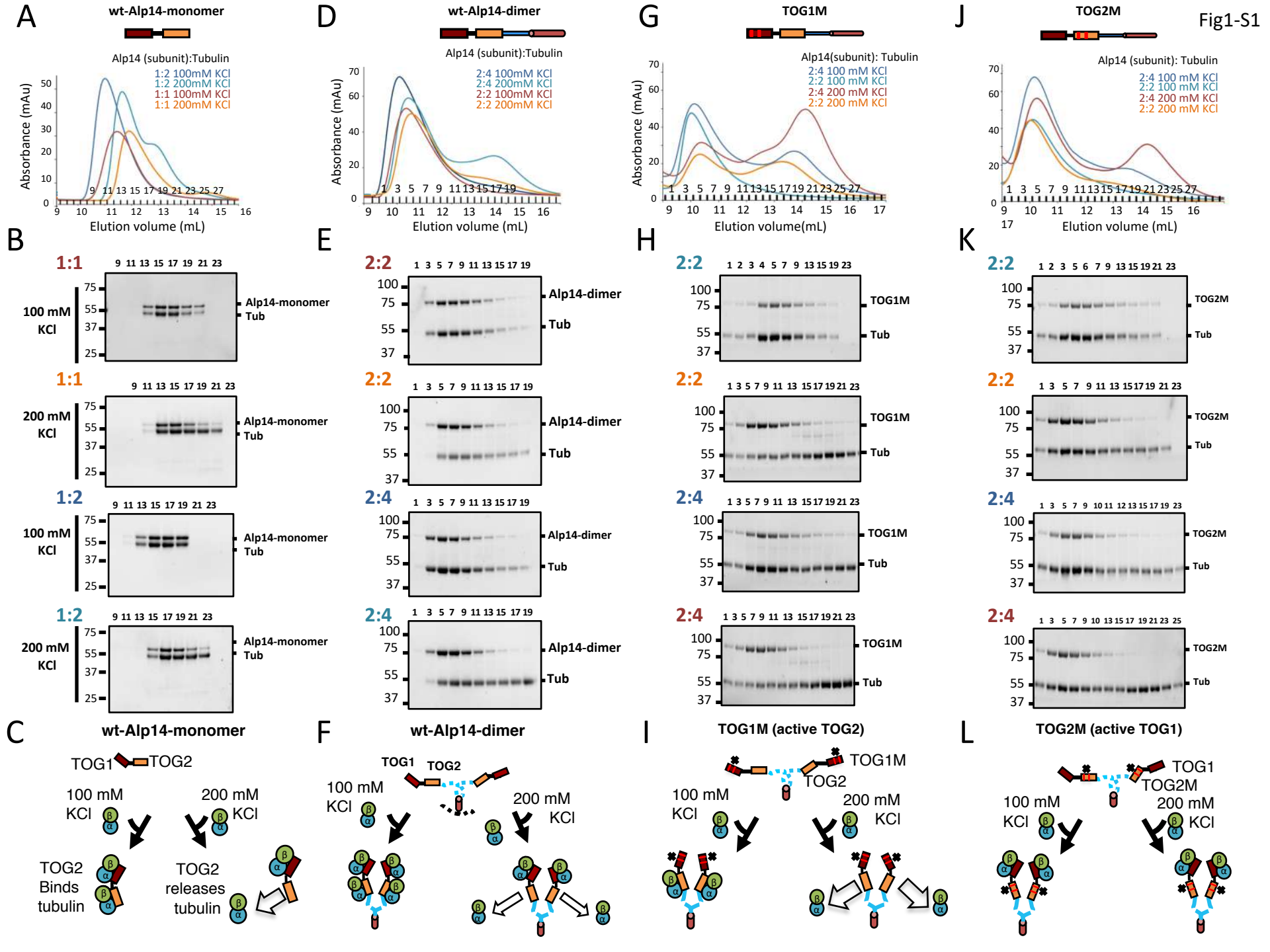
A
wt-Alp14-monomer
Alp14 (subunit):Tubulin
1:2 100mM KCl
1:2 200mM KCl
1:1 100mM KCl
1:1 200mM KCl
Absorbance (mAu)
Elution volume (mL)
D
wt-Alp14-dimer
Alp14 (subunit):Tubulin
2:4 100mM KCl
2:4 200mM KCl
2:2 100mM KCl
2:2 200mM KCl
Absorbance (mAu)
Elution volume (mL)
G
TOG1M
Alp14(subunit): Tubulin
2:4 100 mM KCl
2:2 100 mM KCl
2:4 200 mM KCl
2:2 200 mM KCl
Absorbance (mAu)
Elution volume(mL)
J
TOG2M
Alp14 (subunit): Tubulin
2:4 100 mM KCl
2:2 100 mM KCl
2:4 200 mM KCl
2:2 200 mM KCl
Elution volume (mL)
Fig1-S1
B
1:1
100 mM KCl
1:1
200 mM KCl
1:2
100 mM KCl
1:2
200 mM KCl
Alp14-monomer
Tub
E
2:2
2:2
2:4
2:4
Alp14-dimer
Tub
H
2:2
2:2
2:4
2:4
TOG1M
Tub
K
2:2
2:2
2:4
2:4
TOG2M
Tub
C
wt-Alp14-monomer
TOG1
TOG2
100 mM KCl
200 mM KCl
TOG2 Binds tubulin
TOG2 releases tubulin
F
wt-Alp14-dimer
TOG1
TOG2
100 mM KCl
200 mM KCl
I
TOG1M (active TOG2)
TOG1M
TOG2
100 mM KCl
200 mM KCl
L
TOG2M (active TOG1)
TOG1
TOG2M
100 mM KCl
200 mM KCl

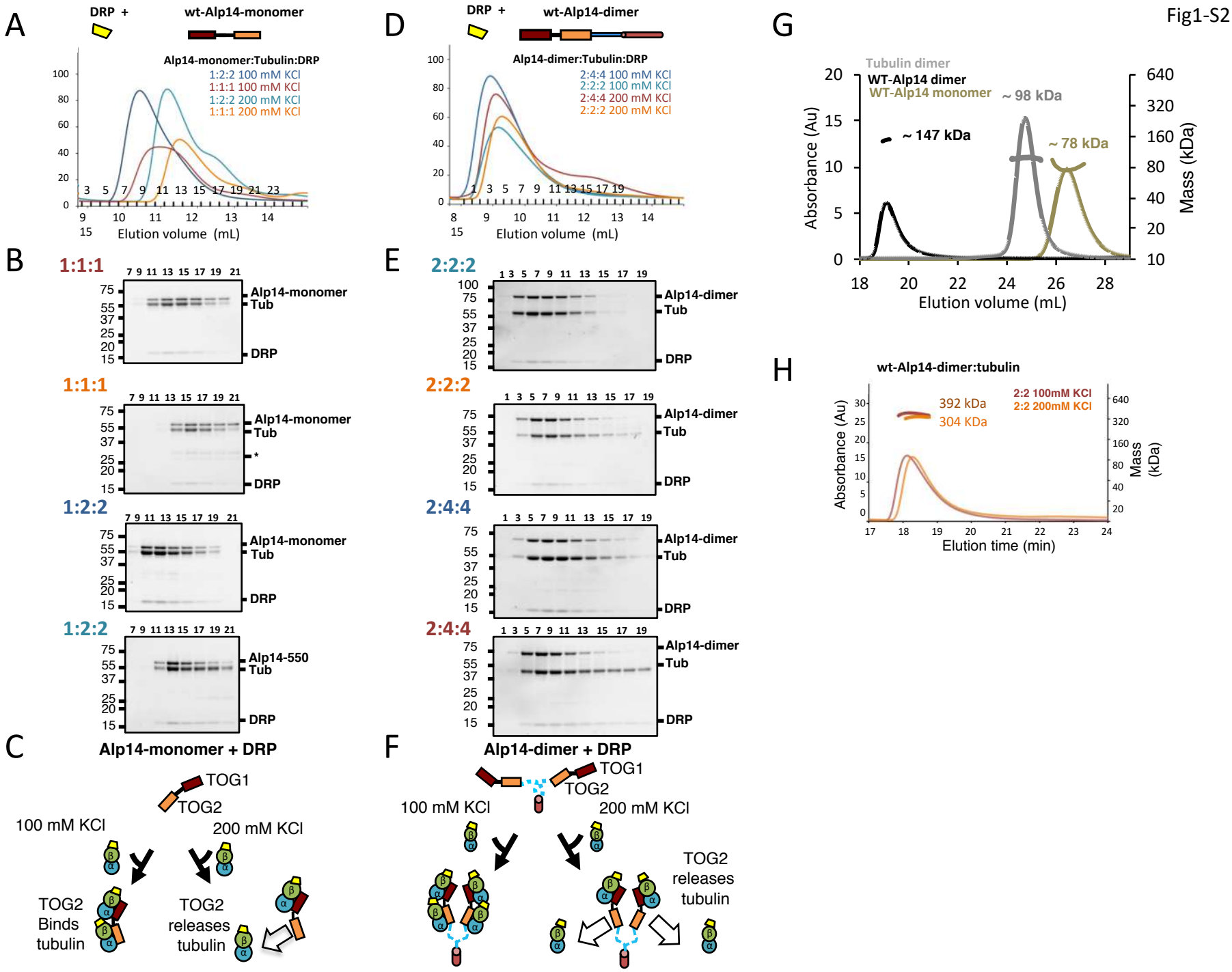
A
DRP +
wt-Alp14-monomer
Alp14-monomer:Tubulin:DRP
1:2:2 100 mM KCl
1:1:1 100 mM KCl
1:2:2 200 mM KCl
1:1:1 200 mM KCl
Elution volume (mL)
D
DRP +
wt-Alp14-dimer
Alp14-dimer:Tubulin:DRP
2:4:4 100 mM KCl
2:2:2 100 mM KCl
2:4:4 200 mM KCl
2:2:2 200 mM KCl
Elution volume (mL)
G
Tubulin dimer
WT-Alp14 dimer
WT-Alp14 monomer
~ 98 kDa
~ 147 kDa
~ 78 kDa
Absorbance (Au)
Mass (kDa)
Elution volume (mL)
H
wt-Alp14-dimer:tubulin
392 kDa
304 kDa
2:2 100mM KCl
2:2 200mM KCl
Absorbance (Au)
Mass (kDa)
Elution time (min)
B
1:1:1
Alp14-monomer
Tub
DRP
1:1:1
Alp14-monomer
Tub
*
DRP
1:2:2
Alp14-monomer
Tub
DRP
1:2:2
Alp14-550
Tub
DRP
E
2:2:2
Alp14-dimer
Tub
DRP
2:2:2
Alp14-dimer
Tub
DRP
2:4:4
Alp14-dimer
Tub
DRP
2:4:4
Alp14-dimer
Tub
DRP
C
Alp14-monomer + DRP
TOG1
TOG2
100 mM KCl
200 mM KCl
TOG2
Binds
tubulin
TOG2
releases
tubulin
F
Alp14-dimer + DRP
TOG1
TOG2
100 mM KCl
200 mM KCl
TOG2
releases
tubulin

A

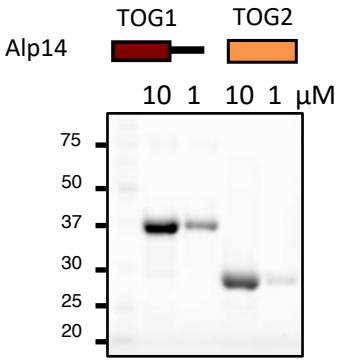

B

KCl (mM)	K_d (nM)	K_d (nM)
100	72.88	173.2
200	1530	3250

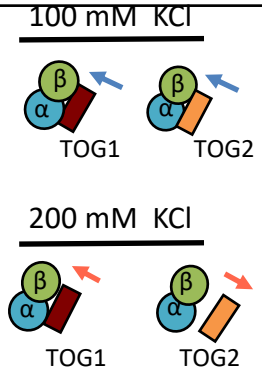

C

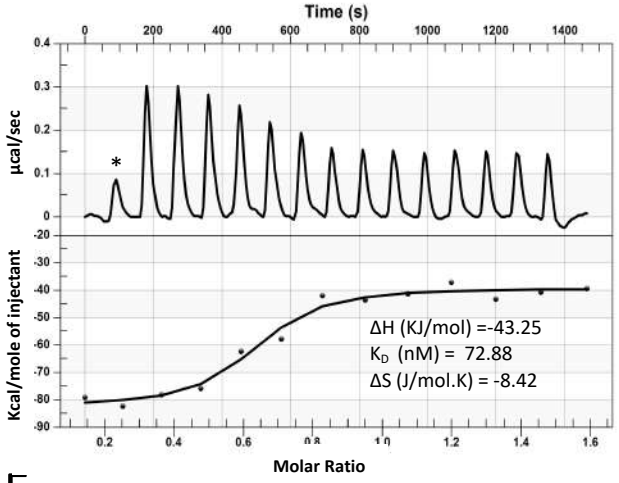

D

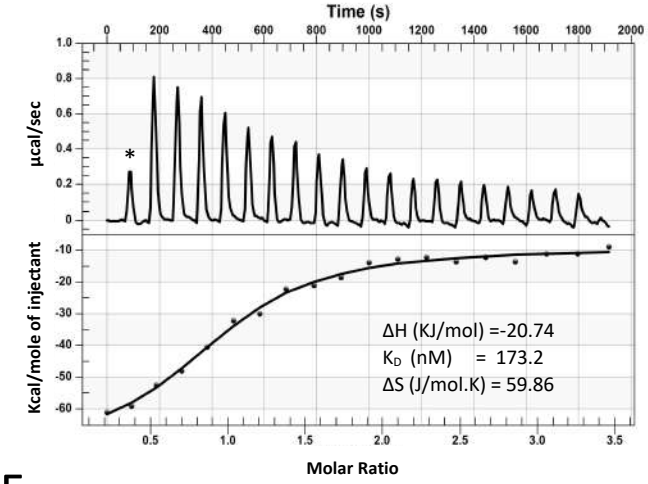

E

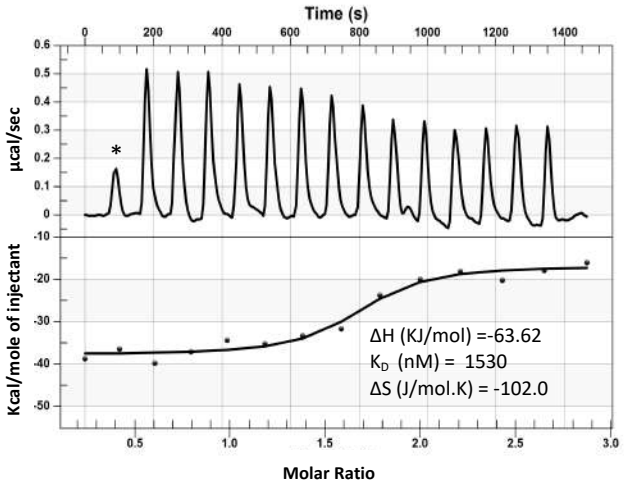

F

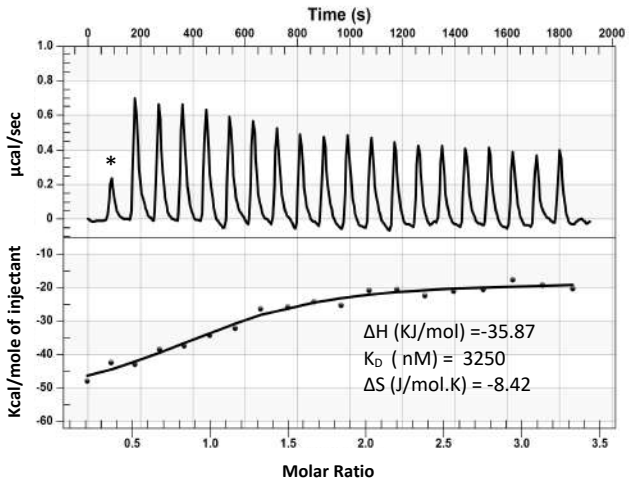

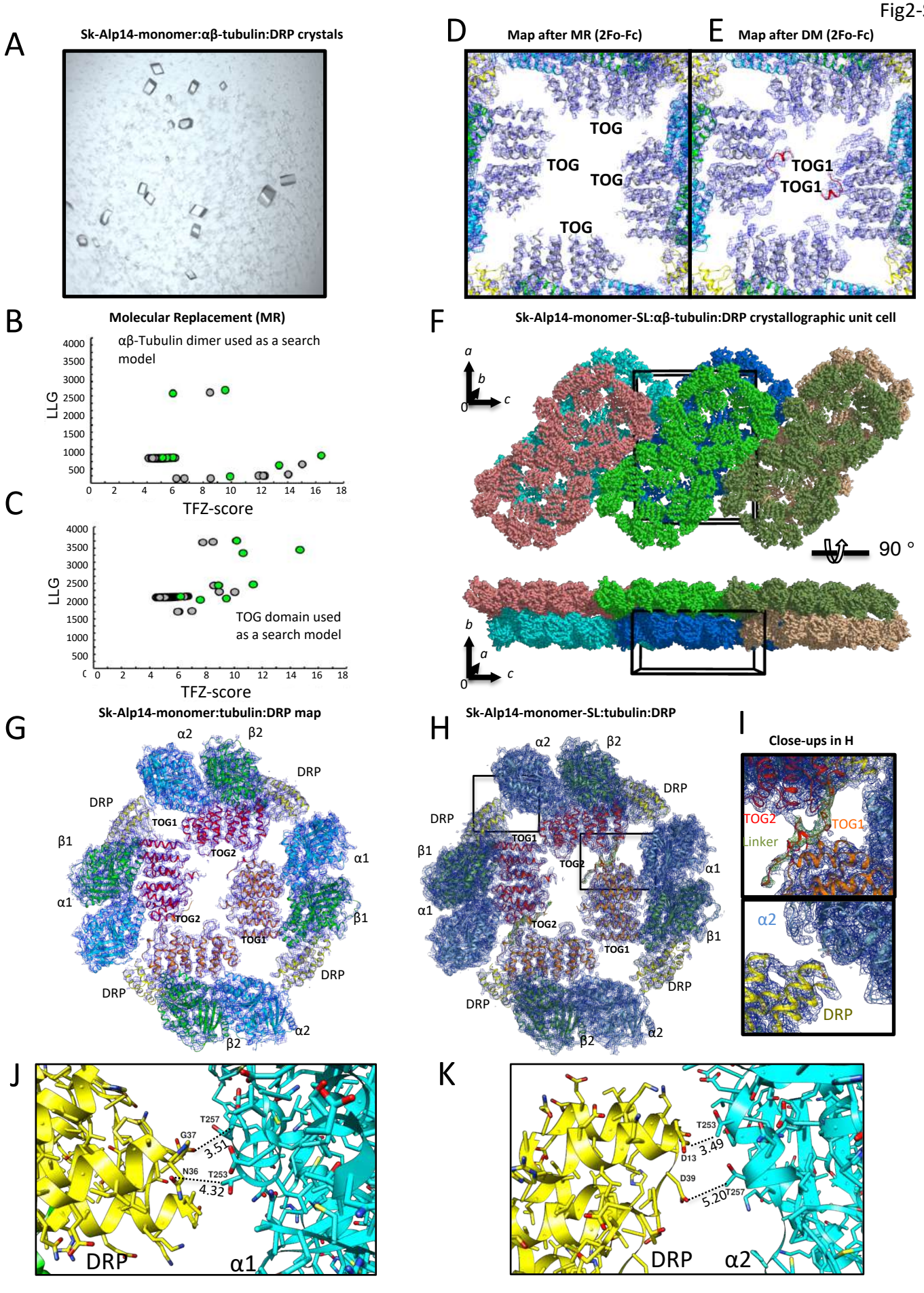
A
Sk-Alp14-monomer:αβ-tubulin:DRP crystals
D
Map after MR (2Fo-Fc)
E
Map after DM (2Fo-Fc)
TOG
TOG
TOG
TOG
TOG1
TOG1
B
Molecular Replacement (MR)
αβ-Tubulin dimer used as a search model
LLG
TFZ-score
C
TOG domain used as a search model
LLG
TFZ-score
F
Sk-Alp14-monomer-SL:αβ-tubulin:DRP crystallographic unit cell
90 °
G
Sk-Alp14-monomer:tubulin:DRP map
α2
β2
DRP
DRP
TOG1
TOG2
β1
α1
α1
TOG2
β1
TOG1
DRP
DRP
α2
β2
H
Sk-Alp14-monomer-SL:tubulin:DRP
α2
β2
DRP
DRP
TOG1
β1
TOG2
α1
α1
TOG2
β1
TOG1
DRP
DRP
β2
α2
I
Close-ups in H
TOG2
TOG1
Linker
α2
DRP
J
T257
G37
3.51
N36
T253
4.32
DRP
α1
K
T253
D13
3.49
D39
5.20
T257
DRP
α2

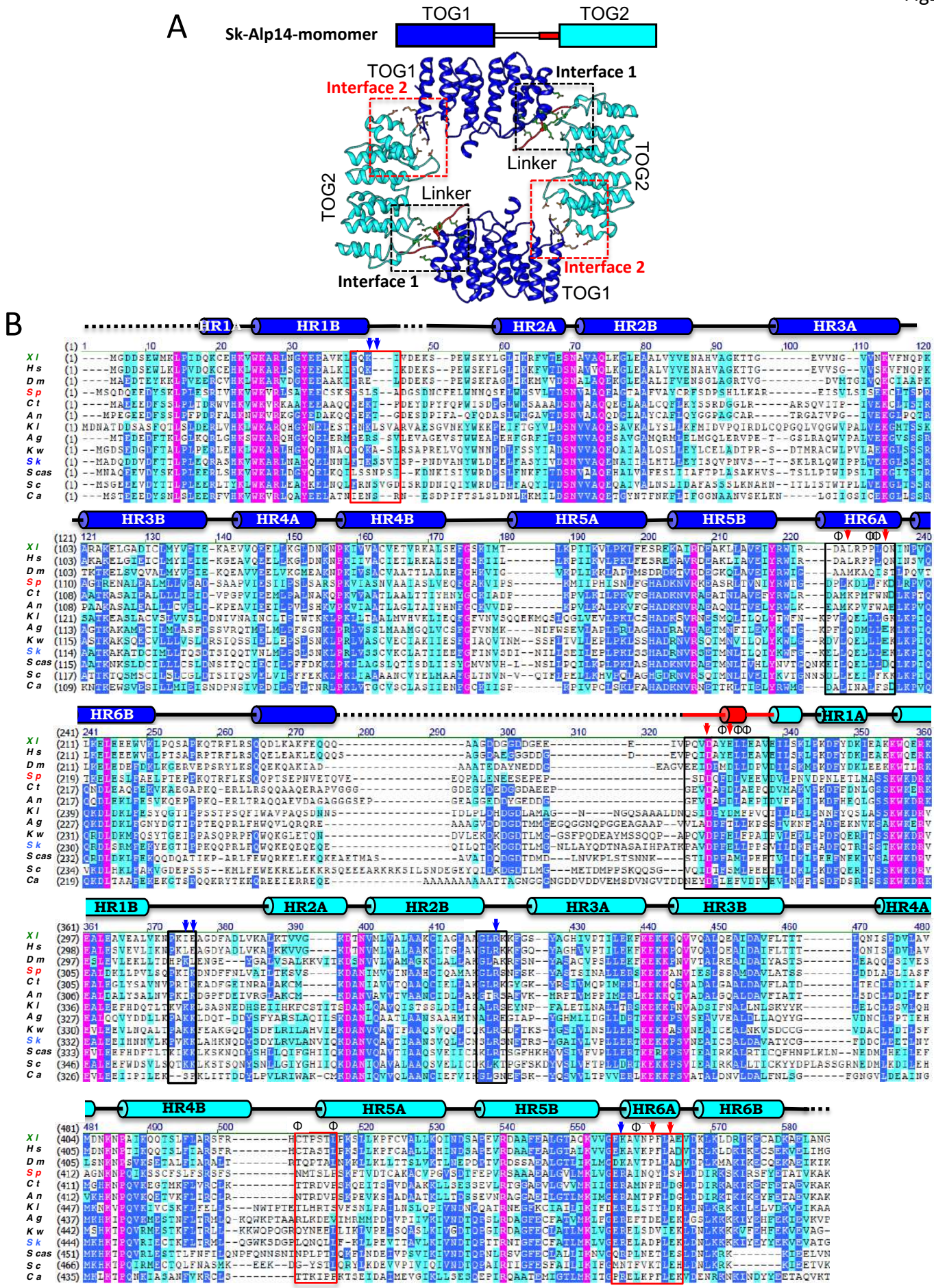
A
Sk-Alp14-momomer
TOG1
TOG2
TOG1
Interface 1
Interface 2
Linker
TOG2
Linker
TOG2
Interface 2
Interface 1
TOG1
B
HR1
HR1B
HR2A
HR2B
HR3A
HR3B
HR4A
HR4B
HR5A
HR5B
HR6A
HR6B
HR1A
Xl
Hs
Dm
Sp
Ct
An
Kl
Ag
Kw
Sk
Scas
Sc
Ca

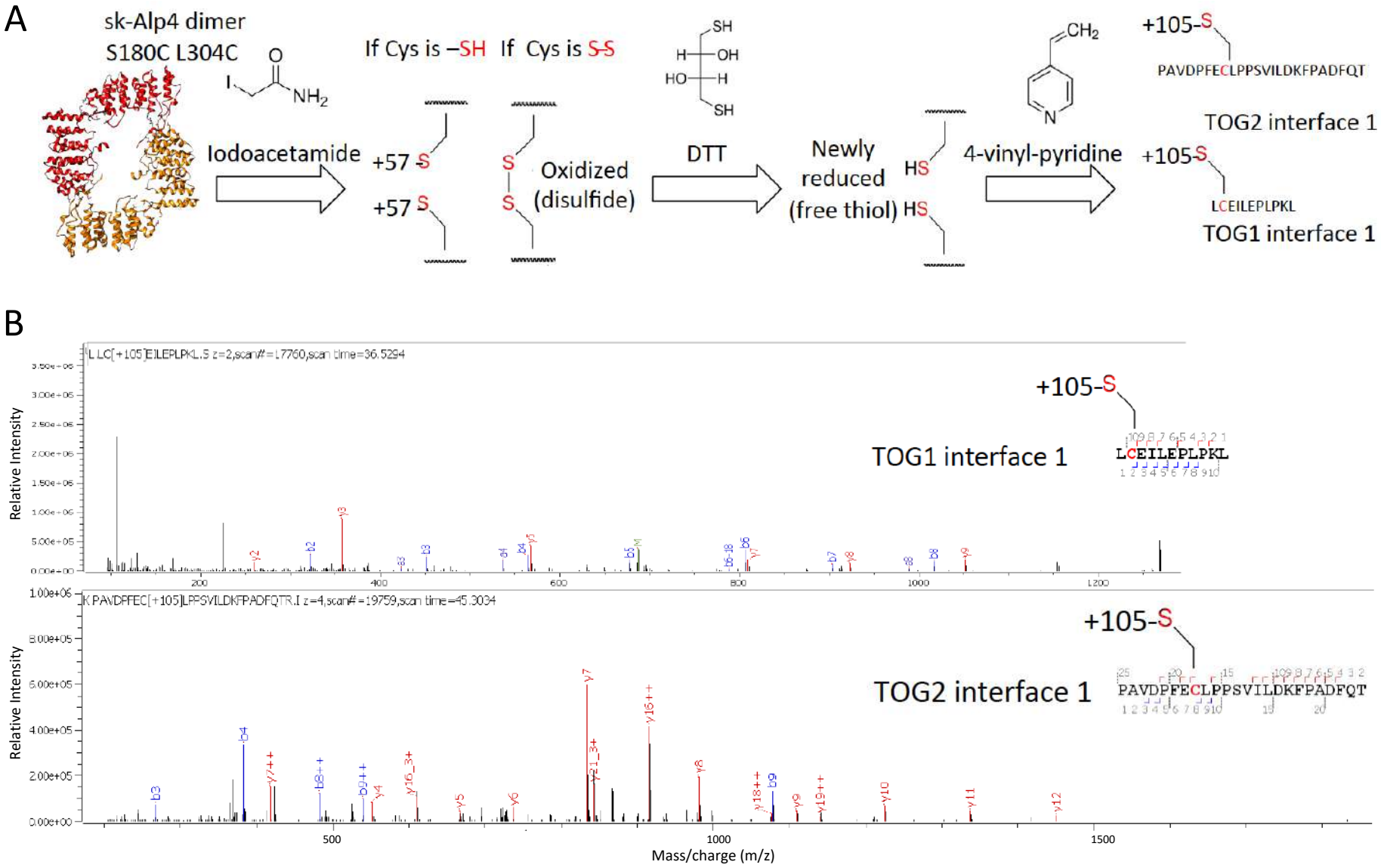
A
sk-Alp4 dimer
S180C L304C
Iodoacetamide
If Cys is –SH
If Cys is S-S
+57
+57
Oxidized
(disulfide)
DTT
Newly
reduced
(free thiol)
4-vinyl-pyridine
+105-S
PAVDPFECLPPSVILDKFPADFQT
TOG2 interface 1
+105-S
LCEILEPLPKL
TOG1 interface 1
B
L.LC[+105]EILEPLPKL.S z=2,scan#=17760,scan time=36.5294
+105-S
TOG1 interface 1
LCEILEPLPKL
Relative Intensity
K.PAVDPFEC[+105]LPPSVILDKFPADFQTR.I z=4,scan#=19759,scan time=45.3034
+105-S
TOG2 interface 1
PAVDPFECLPPSVILDKFPADFQT
Relative Intensity
Mass/charge (m/z)

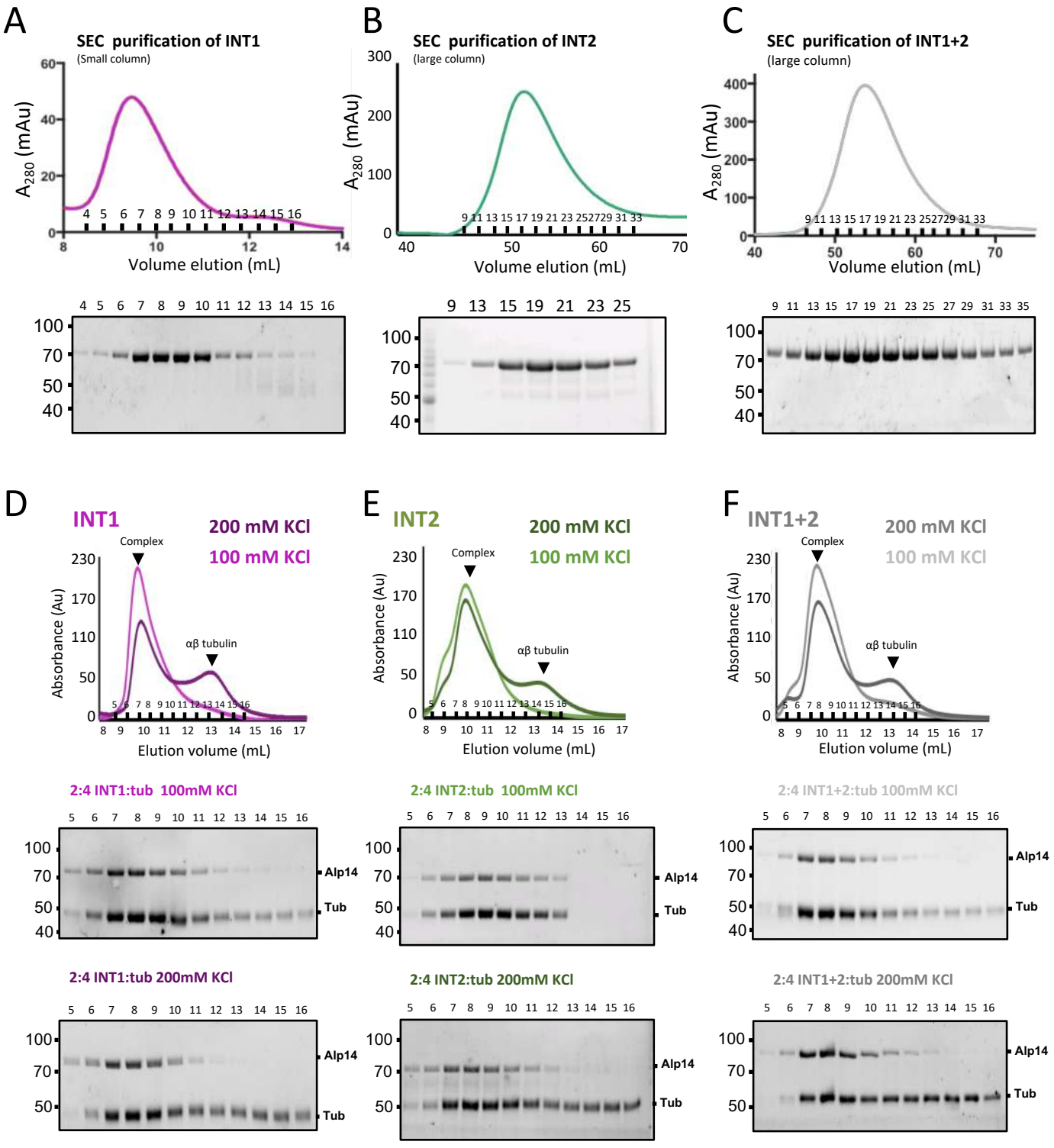
A
SEC purification of INT1
(Small column)
A280 (mAu)
Volume elution (mL)
B
SEC purification of INT2
(large column)
A280 (mAu)
Volume elution (mL)
C
SEC purification of INT1+2
(large column)
A280 (mAu)
Volume elution (mL)
D
INT1
200 mM KCl
100 mM KCl
Complex
αβ tubulin
Absorbance (Au)
Elution volume (mL)
E
INT2
200 mM KCl
100 mM KCl
Complex
αβ tubulin
Absorbance (Au)
Elution volume (mL)
F
INT1+2
200 mM KCl
100 mM KCl
Complex
αβ tubulin
Absorbance (Au)
Elution volume (mL)
2:4 INT1:tub 100mM KCl
2:4 INT2:tub 100mM KCl
2:4 INT1+2:tub 100mM KCl
2:4 INT1:tub 200mM KCl
2:4 INT2:tub 200mM KCl
2:4 INT1+2:tub 200mM KCl
Alp14
Tub

A **WT-Alp14**

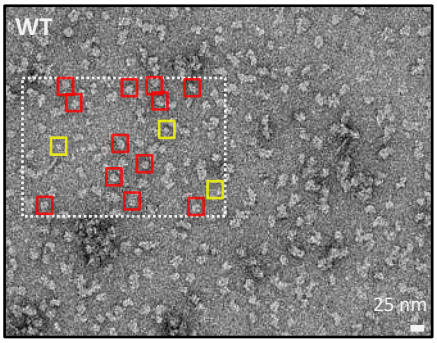

B

TOG-square 4 αβ tubulins (Loaded Wheel)

2D class averages

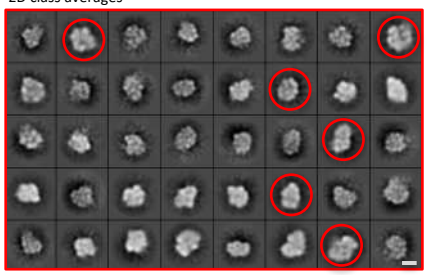

C

TOG square (-αβ tubulins) (empty square)

2D class averages

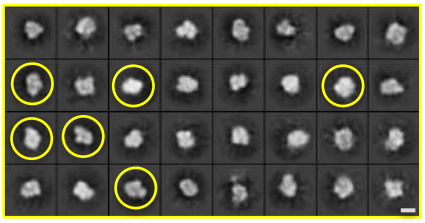

D **INT1**

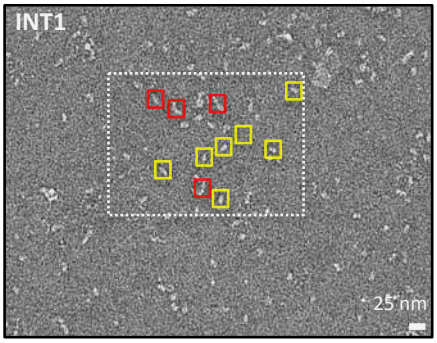

E

Unfurled TOG array

Half-TOG square

Multiple conformations between unfurled TOG array and half-TOG square

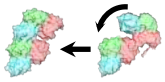

2D class averages

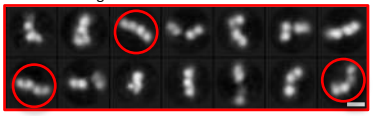

F

Single TOG αβ tubulin

2D class averages

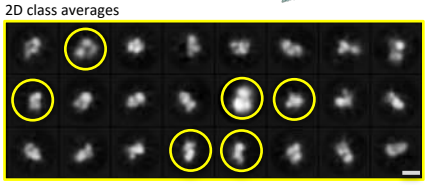

G **INT2**

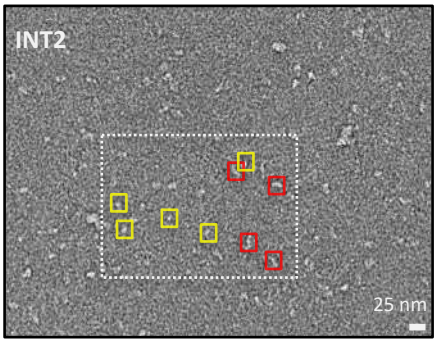

H

Unfurled TOG array

Half-TOG square

Multiple conformations between unfurled TOG array and half-TOG square

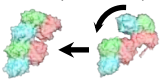

2D class averages

I

Single TOG αβ tubulin

2D class averages

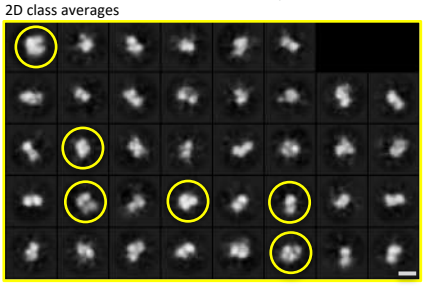

J **INT1+2**

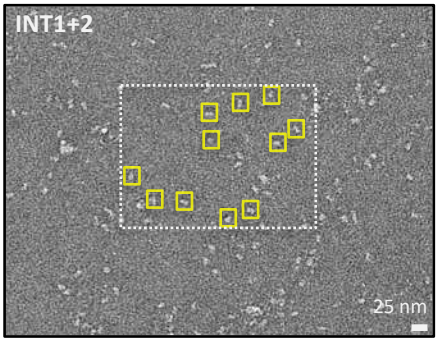

K

Single TOG αβ tubulin

2D class averages

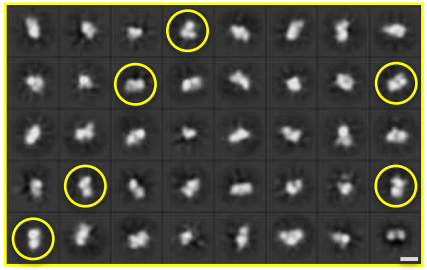

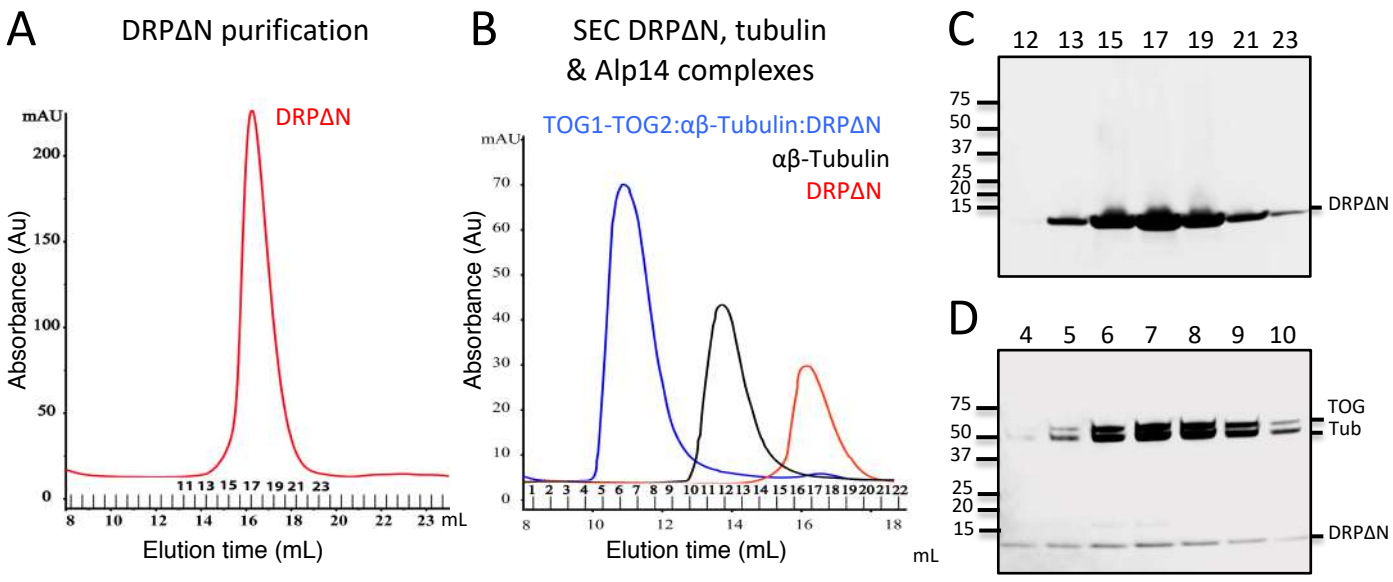
A
DRPΔN purification
DRPΔN
mAU
Absorbance (Au)
Elution time (mL)
B
SEC DRPΔN, tubulin
& Alp14 complexes
TOG1-TOG2:αβ-Tubulin:DRPΔN
αβ-Tubulin
DRPΔN
Absorbance (Au)
Elution time (mL)
mL
C
12 13 15 17 19 21 23
DRPΔN
D
4 5 6 7 8 9 10
TOG
Tub
DRPΔN

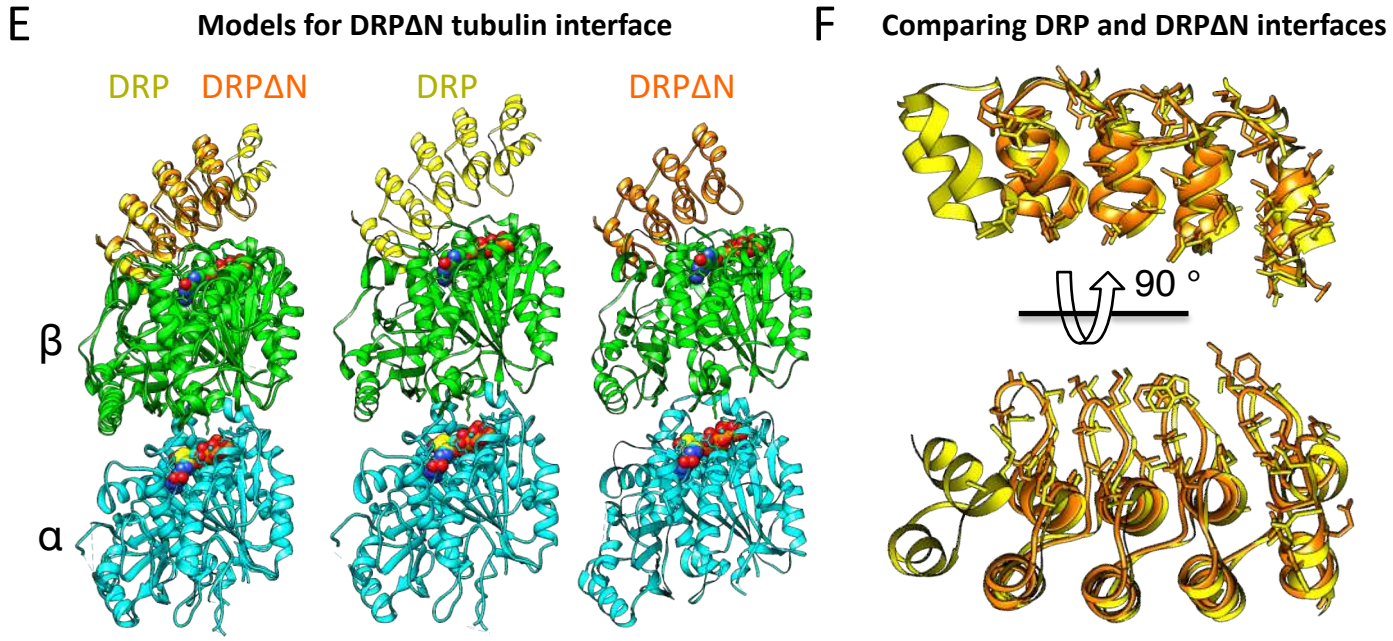
E
Models for DRPΔN tubulin interface
DRP
DRPΔN
DRP
DRPΔN
β
α
F
Comparing DRP and DRPΔN interfaces
90 °

A **Sk-Alp14-monomer:tubulin:DRPΔN crystals**

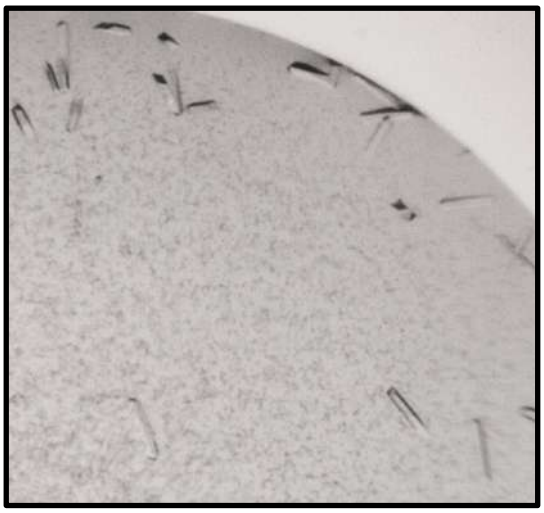

B **Molecular Replacement**

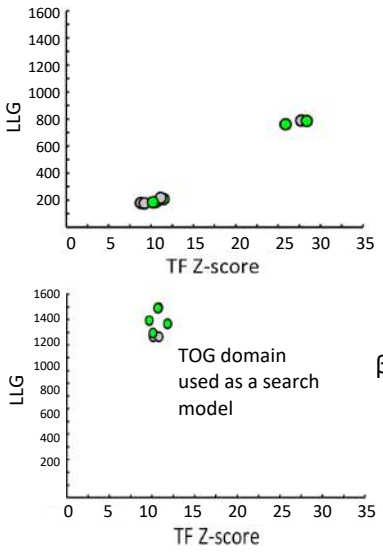

C **Map of 1:2:1 complex**

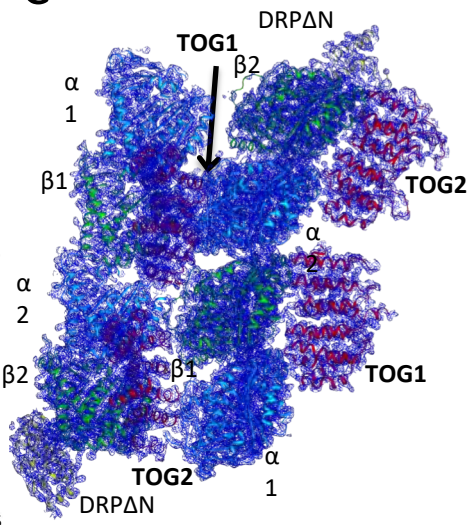

D **Packing in the crystallographic unit cell**

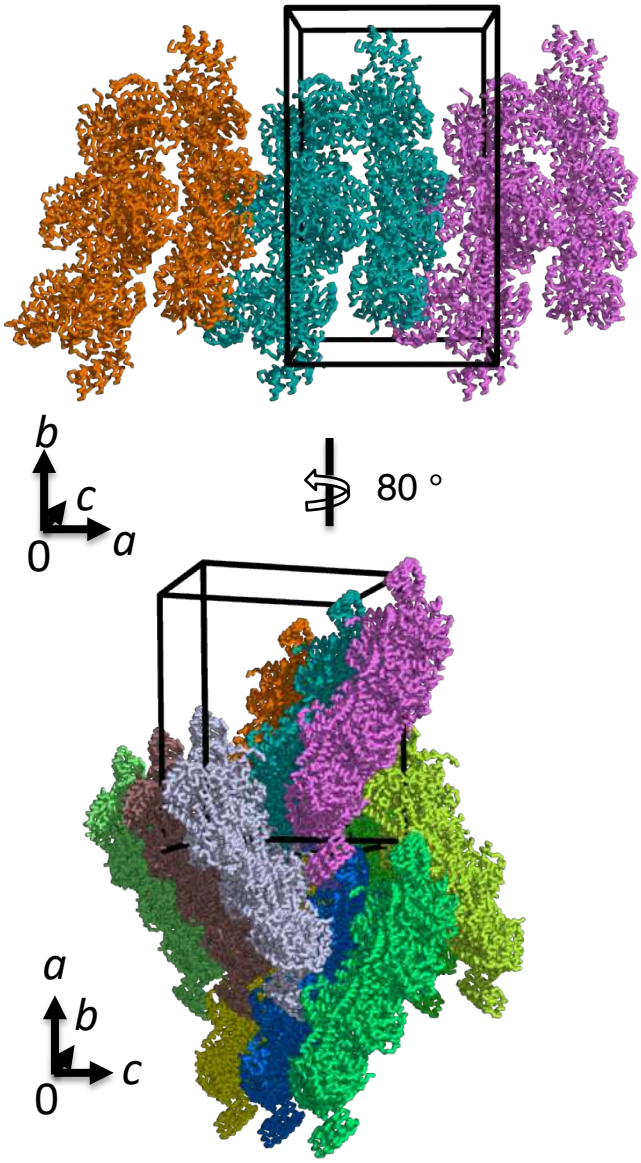

E **αβ-tubulins are highly curved in the Sk-Alp14-monomer:tubulin:DRPΔN structure**

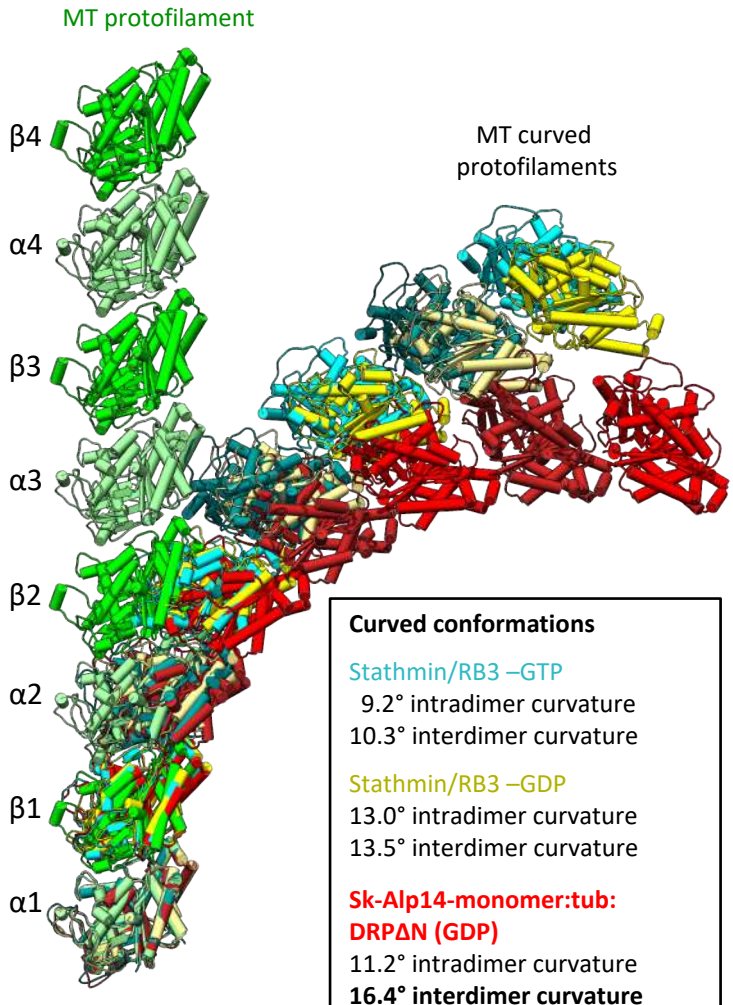

Curved conformations

Stathmin/RB3 –GTP
9.2° intradimer curvature
10.3° interdimer curvature

Stathmin/RB3 –GDP
13.0° intradimer curvature
13.5° interdimer curvature

Sk-Alp14-monomer:tub: DRPΔN (GDP)
11.2° intradimer curvature
16.4° interdimer curvature

A TOG1-docked

B TOG2-docked

C Overlay